THEORETICAL NOTES

Note 363

October 1992

A COMPLETE EMP ENVIRONMENT GENERATED BY HIGH-ALTITUDE NUCLEAR BURSTS

K.D. Leuthäuser
Fraunhofer-Institut für Naturwissenschaftlich-Technische Trendanalysen
Appelsgarten 2, 5350 Euskirchen (Germany)

ABSTRACT

Very few papers are available in the open literature on high-altitude nuclear EMP fields offering detailed quantitative results for the whole variety of weapon related input parameters (i.e. gamma yield, energy and pulse shape) and scenario oriented quantities (i.e. height of burst, observer location with regard to Ground Zero).

The EXEMP code developed by the author is extensively employed for systematic variation of the above mentioned parameters. The code is self-consistent, i.e. solves the equation of motion of the Compton electrons in the presence of EMP generated collective electric and magnetic fields. The basic approximation is still the high-frequency or outgoing-wave approximation of the Maxwell equations in retarded time which are thus reduced to ordinary differential equations.

Equations of motion of Compton electrons, electron density rate equations and Maxwell equations are solved numerically by means of a fourth order Runge-Kutta algorithm. The influence of the various input parameters on the incident electromagnetic fields will be extensively discussed, including 'smile-face' diagrams and plots showing pulse width, power per unit area and polarization dependent on observer location.

TABLE OF CONTENTS

1. INTRODUCTION

Although there is very much knowledge available about EMP environments generated by high-altitude nuclear bursts (HEMP), practically no systematic attempt has become known in the open literature devoted to the whole variability of EMP fields received on the earth surface. C.L. Longmire's paper [1] is one exception, but focusses on the EMP variation with observer location and essentially ignores variation of all other input parameters for which fixed nominal values were used (e.g. weapon yield, height of burst, mean energy of gamma radiation, gamma pulse shape, dip angle and intensity of earth magnetic field).

The main objective of this paper is to close this gap by means of systematic variation of the parameters mentioned above. Another intention is to demonstrate the quantitative influence of various approximations frequently used in HEMP calculations. Examples are the neglection of self-consistency, of the time lag in formation of the secondary ionization, and of electron avalanching as well as the assumption of uniform earth magnetic field and flat earth surface.

To perform the numerical computations the EXEMP code was developed by the present author. In its complete version, EXEMP is self-consistent, i.e. solves the equation of motion of Compton electrons in the presence of EMP fields, and takes the exact three-dimensional energy-scattering angle correlation of the Compton effect into account. The underlying theoretical model is essentially an extension of the original Karzas-Latter-Longmire (KLL) model [2, 3]. In particular, EXEMP is based on the high-frequency or outgoing wave approximation of the Maxwell equations in which, after transformation to retarded time, space derivatives can be neglected with respect to time derivatives. This approximation seems to be well established for early time EMP fields (up to a few hundred nanoseconds as assumed in this paper) and for observer locations not to close to the explosion horizon.

2. SELECTED TOPICS OF THE HEMP GENERATION MODEL

The basic model underlying EXEMP is the Karzas-Latter-Longmire theory [2, 3]. However, many additional features were incorporated into the code to improve the quantitative results. These improvements and supplements are scattered over a vast number of publications and laboratory reports. The most relevant of them are therefore summarized in this section and converted to representations as they appear in EXEMP.

2.1 Equation of Motion of Compton Electrons

If a gamma ray of energy E_γ emitted by the nuclear burst interacts with an electron of the air molecules in a Compton collision, a Compton recoil electron is created at an angle θ with respect to the direction of the incident gamma ray. The conservation laws correlate angle θ and the kinetic energy E_0 of the Compton electron as follows

$$\cos\theta = \frac{1+\alpha}{\alpha}\left(\frac{\gamma_0 - 1}{\gamma_0 + 1}\right)^{1/2} \tag{1}$$

where $\alpha = E_\gamma/mc^2$ is the energy of the incident gamma in terms of the rest mass mc^2 = .511 MeV of the electron and $\gamma_0 = 1+E_0/mc^2$. The maximum energy is obtained in forward direction (θ=0)

$$\gamma_{max} = 1+\frac{2\alpha^2}{1+2\alpha}. \tag{2}$$

The maximum scattering angle is $\theta=\pi/2$, for which γ_0=1.

For given E_γ, the initial conditions for the equation of motion of the Compton electron are thus specified by γ_0 and θ. However, if external forces (e.g. electromagnetic fields $\vec{E}$ and $\vec{B}$) are present, it is necessary also to consider the azimuth angle ϕ of the Compton electron as an initial condition.

The equation of motion for a relativistic electron in an electromagnetic field $(\vec{E},\vec{B})$ is given by

$$m\frac{d}{dt}(\gamma\vec{v}) = -e\vec{E} - e\vec{v}\times\vec{B} - \frac{F(\gamma)}{v^2}\vec{v} \tag{3}$$

where $\vec{E} = \vec{E}(\vec{r},t)$ is the EMP generated electric field, and

$$\vec{B} \rightarrow \vec{B}_0(\vec{r}) + \vec{B}(\vec{r},t)$$

is the sum of the static earth magnetic field and the EMP generated magnetic field.

The last term in Eq. (3) stands for the drag force due to ionization energy loss which in the absence of electric fields is given by the Bethe-Bloch equation

$$mc^2\frac{d\gamma}{dt} = -F(\gamma) \tag{4}$$

where $F(\gamma)$ is proportional to the density of atoms N, the atomic number Z and a complicated function containing γ and the mean excitation potential of air [4].

Introducing dimensionless variables $\vec{u} = \gamma\vec{v}/c$, Eq. (3) can be rewritten as

$$\frac{d\vec{u}}{dt} = -\frac{e}{mc}\vec{E} - \frac{e}{m\gamma}\vec{u}\times\vec{B} - G(\gamma)\,\vec{u} \tag{5}$$

where

$$G(\gamma) = \frac{F(\gamma)}{mc^2\beta^2\gamma}, \qquad \beta = \frac{v}{c} = \left(1-1/\gamma^2\right)^{1/2}$$

and

$$\gamma^2 = 1+\vec{u}^2 .$$

To account for multiple scattering, the obliquity factor η was introduced [4] which relates the differential track length ds to the distance dx in the initial direction. Therefore,

$$\frac{d\vec{r}}{dt} = \frac{\vec{v}}{\eta} \tag{6}$$

where η is determined by the differential equation [4]

$$mc^2(\gamma^2-1)\frac{d\eta}{dt} = 3.874\ F(\gamma)+ec(\eta^2-1)\ \vec{E}\cdot\vec{u} . \tag{7}$$

Eqs. (5) and (7) constitute a system of four ordinary differential equations for the unknown functions $\vec{u}(t)$ and $\eta(t)$. Once these equations are solved, the Compton current contribution of a single Compton electron can readily be obtained

$$\vec{j} = -\frac{e}{c}\frac{d\vec{r}}{dt} = -\frac{e}{c}\frac{\vec{v}}{\eta} = -e\frac{\vec{u}}{\gamma\eta} . \tag{8}$$

The production rate of secondary electrons (i.e. ion pairs) is

$$\frac{dn_{sec}}{dt} = \frac{F(\gamma)}{E_{ion}} = 1{,}5 \times 10^4\ \frac{F(\gamma)}{mc^2} \tag{9}$$

where E_{ion}=34 eV is the energy expended per ion pair in air. Hence, the conductivity produced by an individual Compton electron is

$$\sigma(\vec{r},t) = e\mu(\vec{r},E)\ n_{sec}(r,t)$$

$$= 1{,}5x10^4\frac{e}{mc^2}\ \mu(\vec{r},\vec{E})\int_0^t F(\gamma(t'))\,dt' \tag{10}$$

where μ denotes the electron mobility.

2.2 Coordinate Systems

The numerical solution of the equation of motion in conjunction with the obliquity equation and also the solution of Maxwell equations require the specification of a coordinate system.

Under the assumption of a plane atmosphere and earth surface and of a uniform earth magnetic field B_0 it would be most convenient to introduce right-handed Cartesian coordinates with the z axis in the direction $\bar{r}_0$ of line-of-sight between burst point and observer location on ground, and x in the direction of $-\bar{r}_0 \times \bar{B}_0$. However, if a dipole earth magnetic field is introduced, such a coordin. system could be defined only locally. Therefore, a coordinate system independent of the atmospheric height will be preferred with the z axis as above but the x axis in horizontal direction (i.e. parallel to the earth surface).

In particular, the components of the earth magnetic field must be determined in this coordinate system.

Let B_0 be the magnitude of the earth magnetic field at the height at which the equation of motion has to be solved and let φ_0 be the corresponding dip angle as obtained from the dipole model (see Section 2.8). Then

$$\bar{B}_0 = B_0(0, \cos\varphi_0, -\sin\varphi_0) \tag{11}$$

are the coordinates of the earth magnetic field in a local Cartesian coordinate system attached to the observer, where the x_0- and y_0-axes are in geomagnetically eastward- and northward horizontal directions, respectively, and z_0 is locally upward-vertical. In the same coordinates, the line-of-sight unit vector from the burst point to the observer at height h above ground is

$$\hat{r}_0 = (\cos\varphi \sin\Psi, \sin\varphi \sin\Psi, -\cos\Psi) \tag{12}$$

where φ is the azimuth angle of the observer with respect to the eastward direction in a pol coordinate system attached to Ground Zero, and $\Psi=\Psi(h)$ denotes the angle between line-of-sight and the locally vertical direction at the observer. $\Psi(h)$ will be determined in Section 2.7.

Since by definition $\hat{r}_0$ defines the z-axis,

$$B_{0z} = \bar{B}_0 \cdot \hat{r}_0 = B_0(\sin\varphi \cos\varphi_0 \sin\Psi + \sin\varphi_0 \cos\Psi). \tag{13}$$

The unit vectors in $\hat{x}$ and $\hat{y}$ direction are

$$\hat{x} = (\sin\varphi, -\cos\varphi, 0) \tag{14}$$

$$\hat{y} = \hat{z} \times \hat{x} \equiv \hat{r}_0 \times \hat{x} = -(\cos\varphi \cos\Psi, \sin\varphi \cos\Psi, \sin\Psi) \tag{15}$$

respectively, and therefore

$$B_{0x} = -B_0 \cos\varphi \cos\varphi_0 \tag{16}$$

$$B_{0y} = -B_0(\sin\varphi \cos\varphi_0 \cos\Psi - \sin\varphi_0 \sin\Psi) . \tag{17}$$

For an observer position northward or southward of Ground Zero, we have $\varphi = \pm\pi/2$, respectively.

Hence

$$B_{0x} = 0 \tag{18}$$

$$B_{0y} = \mp B_0 \cos(\varphi_0 \pm \Psi) \tag{19}$$

$$B_{0z} = B_0 \sin(\varphi_0 \pm \Psi) . \tag{20}$$

If, furthermore, the observer location y_0 with respect to Ground Zero is such that the line-of-sight vector $\hat{r}_0$ is in the direction of $\vec{B}_0$, i.e. $y_0 = \text{HOB} \cot\varphi_0$, then $\varphi_0 + \Psi = \pi/2$, and

$$\vec{B}_0 = (0, 0, -B_0) . \tag{21}$$

A second distinguished observer location is $y_0 = -\text{HOB tg}\,\varphi_0$ for which $\vec{r}_0$ is perpendicular to $\vec{B}_0$. Because of $\Psi = \varphi_0$, we then have

$$\vec{B}_0 = (0, B_0, 0). \tag{22}$$

Strictly speaking, Eqs. (21) and (22) hold exactly only for a flat earth and atmosphere and a uniform earth magnetic field. If this is not the case, Eqs. (21) and (22) can be satisfied only locally, i.e. for a certain height h.

A third case of interest is the observer vertically underneath the burst point for which $\Psi(h)=0$ is independent of height, and

$$\vec{B}_0 = B_0(0, \cos\varphi_0, \sin\varphi_0) . \tag{23}$$

The solution of the equation of motion (5) together with the obliquity equation (7) also requires the initial values in the coordinate system described above. These are

$$u_x(0) = \gamma_0\beta_0 \sin\theta\cos\phi \tag{24}$$

$$u_y(0) = \gamma_0\beta_0 \sin\theta \sin\phi \tag{25}$$

$$u_z(0) = \gamma_0\beta_0 \cos\theta \tag{26}$$

$$\eta(0) = 1 \tag{27}$$

where γ_0, β_0 and θ are interrelated through Eq. (1), and ϕ denotes the azimuth angle of the Compton electron.

2.3 Compton Currents and Conductivities

Following [2], the production rate of Compton electrons will be written as a product of two functions with seperable variables r (radius vector from burst point to observer location) retarded time $\tau = t - r/c$

$$\dot{n}_c(r,t) = g(r)\, f(t - r/c) \tag{28}$$

where $f(\tau)$ is the source function and $g(r)$ is proportional to the unscattered gamma flux

$$g(r) = \frac{N_0}{4\pi r^2 \lambda(r)} \exp\left(-\int_0^r \frac{dr'}{\lambda(r')} \right) \tag{29}$$

with λ as the total Compton length, and

$$N_0 = \frac{Y_\gamma}{E_\gamma} \tag{30}$$

as the number of gammas of an average gamma-ray energy E_γ, if the total gamma energy yield of the burst is denoted by Y_γ.

For the numerical treatment it is convenient to introduce the atmospheric height h instead of slant range r as the independent variable. In Section 2.7 it will be shown that

$$\hat{r} = \cos\Psi_0 - \sqrt{\cos^2\Psi_0 - (\hat{H}_0 - \hat{h})(2 - \hat{H}_0 + \hat{h})} \tag{31}$$

where the roof quantities are in terms of $R_E + H_0$ (with R_E as the earth radius) and Ψ_0 is the angle between the radius vector and the local vertical direction at the burst point. Hence,

$$\frac{dr}{dh} = -\frac{1 - (\hat{H}_0 - \hat{h})}{\sqrt{\cos^2\Psi_0 - (\hat{H}_0 - \hat{h})(2 - \hat{H}_0 + \hat{h})}} \,. \tag{32}$$

In the plane earth surface and atmosphere approximation

$$r = \frac{H_0 - h}{\cos\Psi_0}, \quad dr = \frac{dh}{\cos\Psi_0} \,. \tag{33}$$

The Compton length $\lambda(h)$ is related to its value $\lambda_0 = \lambda(0)$ at ground by

$$\lambda(h) = \lambda_0\, e^{h/h_0} \tag{34}$$

where h_0 is the atmospheric scale height. This completes the evaluation of g(r).

The time dependent source function $f(\tau)$ must be normalized. From a physical point of view the most appropriate simple analytic expression would be given by

$$f(t) = \frac{\pi}{(\alpha+\beta)\sin\left(\pi\frac{\alpha}{\alpha+\beta}\right)} \quad \frac{1}{e^{-\alpha t}+e^{\beta t}} \tag{35}$$

(sometimes referred to as QEXP = quotient of the sum of two exponentials).

For the reason of comparability of numerical results, also Longmire's decaying step function [1] will be used

$$f(t) = u(t)\,\beta\,e^{-\beta t}\,. \tag{36}$$

For a specific atmospheric height, the Compton current densities are now derived by convolution of the source function Eq. (28) with the current density generated by an individual Compton electron as calculated from Eqs. (3) to (8). Subsequently, these currents must be averaged over the azimuth angles ϕ and energy distributions of the Compton electrons.

The convolution integral is [2]

$$\bar{J}_c(r,t;\phi,\gamma_0) = -eg(r)\int_0^{\infty}\frac{\bar{v}(\tau')}{\eta(\tau')}f\left(t-\frac{r}{c}-\tau'+\frac{1}{c}\int_0^{\tau'}\frac{v_z(\tau'')}{\eta(\tau'')}d\tau''\right)d\tau'\,. \tag{37}$$

Introducing retarded time $\tau = t - r/c$ and the new integration variable

$$\tau_0 = \tau' - \frac{1}{c}\int_0^{\tau'}\frac{v_z(\tau'')}{\eta(\tau'')}d\tau'' \tag{38}$$

$$d\tau_0 = \kappa(\tau')d\tau', \qquad \kappa(\tau') = 1 - \frac{v(\tau')}{c\eta(\tau')} \tag{39}$$

Eq. (37) yields

$$\bar{J}_c(r,\tau;\phi,\gamma_0) = -eg(r)\int_0^{\infty}\frac{\bar{v}(\tau'(\tau_0))}{\eta(\tau'(\tau_0))}f(\tau-\tau_0)\,\frac{d\tau_0}{\kappa(\tau'(\tau_0))}\,. \tag{40}$$

This particular representation of the Compton current implies that the equation of motion of the Compton electrons can most conveniently be integrated in retarded time

$$\frac{d\bar{u}}{d\tau_0} = \frac{d\bar{u}}{d\tau'}\frac{d\tau'}{d\tau_0} = \frac{1}{\kappa(\tau'(\tau_0))}\frac{d\bar{u}}{d\tau'} \tag{41}$$

and similarly for the obliquity equation.

The averages over azimuth angle ϕ and energy γ_0 of the Compton electrons are performed as follows

$$\vec{J}_c(r,\tau) = \overline{\vec{J}_c(r,\tau;\phi,\gamma_0)} \tag{42}$$

$$= \frac{1}{2\pi\,\sigma_c\,(E_\gamma)} \int_0^{2\pi} d\phi \int_0^{\gamma_{max}} d\gamma_0 \frac{d\sigma_c}{d\gamma_0}\,\vec{J}_c(r,\tau;\phi,\gamma_0)$$

$$= -eg(r) \int_0^{\infty} \overline{\left(\frac{\vec{v}}{\eta\kappa}\right)}_{\tau'(\tau_o)} f(\tau-\tau_0)d\tau_0$$

where σ_c and $d\sigma_c/d\gamma_0$ are the total and differential Compton cross sections for an incident gamma ray of energy E_γ, respectively. Exact analytic expressions were taken from [5].

The analogous expression for the conductivity is

$$\sigma(r,\tau) = e\,g(r)\,\mu(r,E) \int_0^{\infty} \overline{\left(\frac{n_{sec}}{\kappa}\right)}_{\tau'(\tau_0)} f(\tau-\tau_0)d\tau_0 \tag{43}$$

where again n_{sec} is evaluated in retarded time

$$\frac{dn_{sec}}{d\tau_0} = \frac{1}{\kappa(\tau'(\tau_0))}\,\frac{dn_{sec}}{d\tau'}$$

$$n_{sec}(\tau'(\tau_0)) = 1.5\text{x}10^4 \int_0^{\tau_0} \left.\frac{F(\gamma)}{\kappa}\right|_{\tau'(\tau_0')} d\tau_0' \,. \tag{44}$$

2.4 High-Frequency Approximation of Maxwell Equations

The calculation of early-time high-altitude EMP fields can greatly be simplified by introducing the high-frequency or outgoing wave approximation because Maxwell equations can be reduced to ordinary differential equations.

Defining $\vec{J}$ as the sum of Compton and conductivity currents

$$\vec{J}(\vec{r},t) = \vec{J}_c(\vec{r},t) + \sigma(\vec{r},t;\vec{E})\,\vec{E}(\vec{r},t) \tag{45}$$

and eliminating $\vec{B}$ from the Maxwell equations

$$\vec{\nabla}\times\vec{B} = \frac{1}{c^2}\frac{\partial\vec{E}}{\partial t} + \mu_0\vec{J} \tag{46}$$

$$\vec{\nabla}\times\vec{E} = -\frac{\partial\vec{B}}{\partial t} \tag{47}$$

yields

$$-\vec{\nabla}\times(\vec{\nabla}\times\vec{E}) = \frac{1}{c^2}\frac{\partial^2\vec{E}}{\partial t^2} + \mu_0\frac{\partial\vec{J}}{\partial t} \tag{48}$$

or, equivalently,

$$-\vec{\nabla}\vec{\nabla}\cdot\vec{E} + \nabla^2\vec{E} = \frac{1}{c^2}\frac{\partial^2\vec{E}}{\partial t^2} + \mu_0\frac{\partial\vec{J}}{\partial t}\,. \tag{49}$$

Adopting again the right-handed rectangular Cartesian coordinates (x,y,z) as introduced in Section 2.2 where z is in the radial (or r) direction, and introducing retarded time

$$\tau = t-\frac{z}{c}\,, \tag{50}$$

the z-derivative has to be replaced by

$$\frac{\partial}{\partial z}\rightarrow\frac{\partial}{\partial z} - \frac{1}{c}\frac{\partial}{\partial\tau}\,. \tag{51}$$

In the high-frequency approximation, partial derivatives at constant retarded time t are considered small compared to derivatives with respect to τ.

The transverse components of Eq. (49) therefore become

$$\frac{\partial E_z}{\partial x} - 2\frac{\partial E_x}{\partial z} = \mu_0 c\, J_x \tag{52}$$

$$\frac{\partial E_z}{\partial x} - 2\frac{\partial E_y}{\partial z} = \mu_0 c\, J_y \tag{53}$$

whereas the longitudinal component will read as

$$\frac{\partial E_z}{\partial\tau} = \mu_0 c^2\, J_z\,. \tag{54}$$

At this stage it cannot yet be decided whether the derivatives of E_z with respect to x and y can be neglected in Eqs. (52) and (53) except for the case, where the observer location is vertically underneath the burst point. They will considerably increase as the observer location approaches the explosion horizon. However, by differentiating Eq. (52) with respect to τ and Eq. (54) with resp to x, E_z can be eliminated, and the following equation is obtained

$$-2\,\frac{\partial^2 E_x}{\partial z d\tau} = \mu_0 c\left(\frac{\partial J_x}{\partial \tau} + \frac{\partial J_z}{\partial x}\right). \tag{55}$$

Assuming now

$$\frac{\partial J_x}{\partial \tau} >> \frac{\partial J_z}{\partial x} \tag{56}$$

reconstitutes the basic high-frequency approximation equation for the transverse electric field as derived in [3] by means of a simplified geometry (i.e. planar gamma ray pulse in vertical direction)

$$2\,\frac{\partial E_i}{\partial z} + \mu_0 c\, J_i = 0, \quad i = x,y\,. \tag{57}$$

The fact that the transverse derivatives of E_z can be omitted in Eqs. (52) and (53) also indicates that in general

$$E_x << E_x, E_y\,. \tag{58}$$

Therefore, even in the deposition layer the electromagnetic wave is almost transverse, and there is no need for solving Eq. (54). Consequently, E_z is also neglected in the equation of motion (5) to (7). Hence, the magnetic field vector is given by

$$\vec{B} = \frac{1}{c}\,(E_y,\ -E_x,\ 0)$$

as in the case of a freely propagating electromagnetic wave.

The EXEMP code uses Eq. (57) not in planar geometry but in more appropriate spherical coordinates [2,3]

$$2\,\frac{\partial}{\partial r}(rE_i) + \mu_0 c\, rJ_i = 0, \quad i = x,y\,. \tag{59}$$

2.5 Ionization Build-up

As confirmed by numerical calculations, a substantial improvement of EXEMP will be achieved by including the effect of the time lag in formation of the secondary ionization.

The quantitative description of the correction term will be as derived in Ref [4]. The result is a modification of the conductivity σ given by Eq. (43) as follows

$$\sigma(r,\tau) \rightarrow \int_{-\infty}^{\tau} H(r,\tau-\tau')\,\sigma(r,\tau')\,d\tau' \tag{60}$$

where

$$H(r,\tau) = H^*(r,\tau) = \frac{34}{86}\left[1+0.160\ell n(1+3.32\times10^{12}\frac{\rho}{\rho_0}\tau)\right] \quad \text{if } H^* < 1$$

$$H(r,\tau) = 1, \quad \text{if } H^* \geq 1 \tag{61}$$

and $\rho/\rho_0 = \exp(-h/h_0)$ is the relative air density as given by the barometric equation.

2.6 Electron Avalanching

Since the effect of electron avalanching on the EMP fields arriving at the earth surface is difficult to estimate, it will be introduced prophylacticly.

Taking avalanching into account the rate equation of the secondary electron number densitiy is [6]

$$\frac{dN_{sec}}{dt} = \dot{N}(t) + \alpha_{av}\,\mu\,E\,N_{sec} \tag{62}$$

where $\dot{N}$ is the rate of secondary electron production caused by the Compton electrons, and α_{av} and μ denote the avalanche coefficient and electron mobility, respectively, both dependent on the total electric field E and the air density at the height under consideration.

Because the EXEMP code due to reasons of computation time does not evaluate $\dot{N}$ but N as given by Eq. (43)

$$N(r,\tau) = \frac{\sigma(r,\tau)}{e\,g(r)\,\mu(r,E)} \tag{63}$$

the following alternate differential equation for $\Delta N = N_{sec}(t)-N(t)$ will be solved

$$\frac{d(\Delta N)}{dt} = \alpha_{av}\mu E\,(\Delta N + N) \tag{64}$$

for each value of r or h.

Because of

$$\lim_{t\rightarrow-\infty} E(t) = \lim_{t\rightarrow-\infty} N(t) = 0$$

the initial value is

$$\Delta N(-\infty) = N_{sec}(-\infty) - N(-\infty) = 0 \ . \tag{65}$$

The dependencies of α_{av} and μ on ρ/ρ_0 and E can only be determined experimentally [6, 7]. However, the following scaling law applies

$$\alpha_{av}\mu E = \frac{\rho}{\rho_0}\,\bar{\alpha}_{av}\,(E\,\frac{\rho_0}{\rho}) \ . \tag{66}$$

Hence $\bar{\alpha}_{av}$ depends on $y = E\rho_0/\rho$ only.

For sufficiently large values of y

$$\bar{\alpha}_{av} \propto y^{2.5}$$

and the influence of avalanche becomes quite substantial for heights above some 40 km. Numerical results are given in Section 3.

2.7 Spherical Earth Surface and Atmosphere

In this section, some geometrical relations will be derived which are necessary to describe the curvature of earth surface and atmosphere.

The geometry is shown in the following figure (see page 13), where Ψ_0 denotes the angle between the radius vector and the local vertical direction at the burst point, whereas $\Psi(r)$ is the corresponding angle at a distance r from the burst point. R_E is the earth radius, h the atmosphereric height above ground, and H_0 the height of burst.

From the figure it follows that

$$h = -R_E + \left(r^2 \sin^2\Psi_0 + (R_E + H_0 - r\cos\Psi_0)^2\right)^{\frac{1}{2}} \ . \tag{67}$$

Introducing dimensionless quantities

$$\hat{h} = \frac{h}{R_E + H_0} \quad \text{and} \quad \hat{r} = \frac{r}{R_E + H_0}$$

and solving Eq. (67) for $\hat{r}$ yields

$$\hat{r} = \cos\Psi_0 - \sqrt{\cos^2\Psi_0 - (\hat{H}_0 - \hat{h})(2 - \hat{H}_0 + \hat{h})}. \tag{68}$$

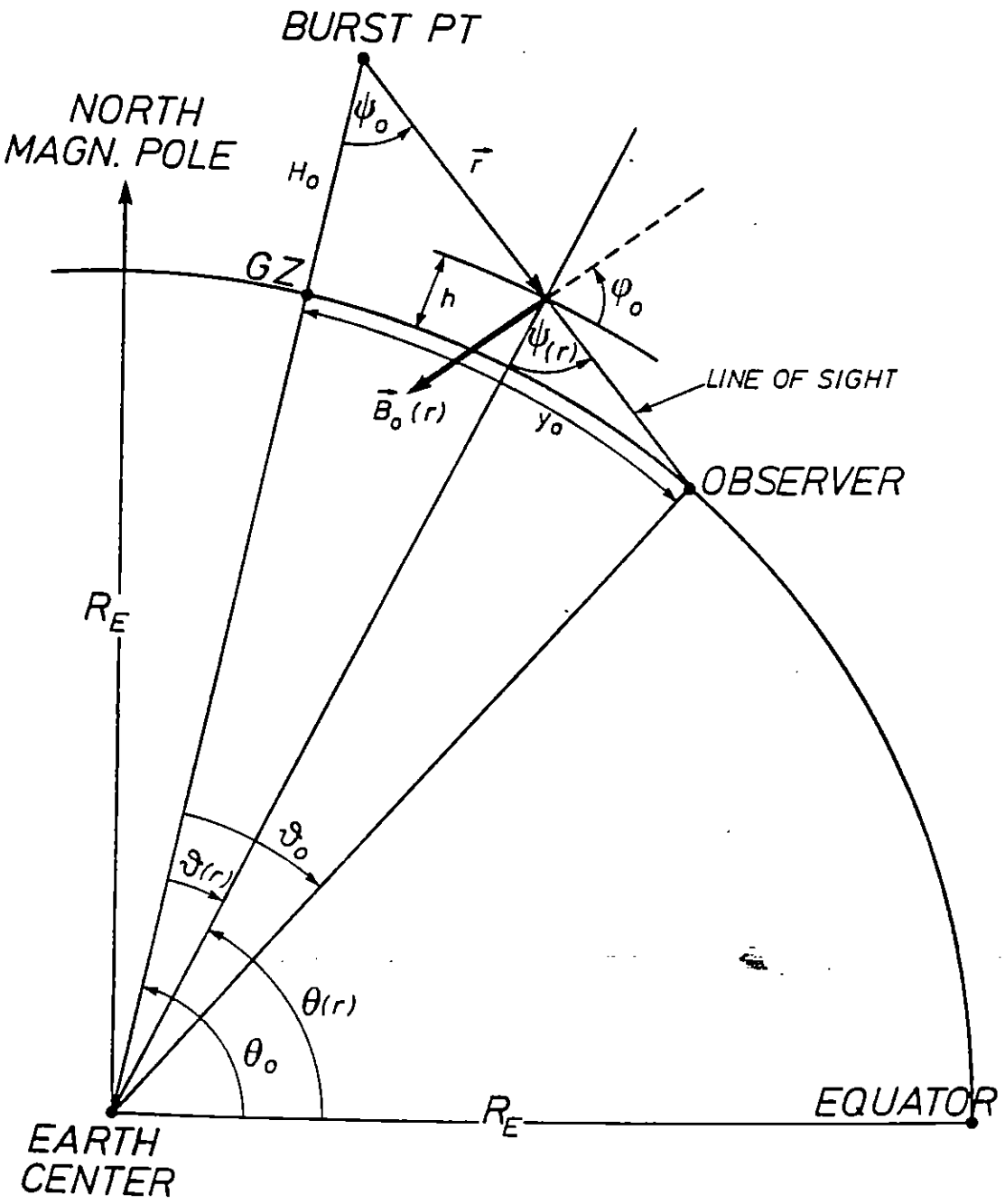
BURST PT
NORTH
MAGN. POLE
ψ_o
H_o
$\vec{r}$
GZ
h
φ_o
$\psi_{(r)}$
LINE OF SIGHT
$\vec{B}_o(r)$
y_o
OBSERVER
R_E
ϑ_o
$\vartheta(r)$
$\theta(r)$
θ_o
R_E
EQUATOR
EARTH
CENTER

The angles Ψ_0 and $\Psi(r)$ are interrelated by

$$\Psi(r) = \frac{\pi}{2} + \Psi_0 - \arctan \frac{1 - \hat{r} \cos \Psi_0}{\hat{r} \sin \Psi_0} . \tag{69}$$

Furthermore, the corresponding angle at the center of the earth is

$$\vartheta(r) = \Psi(r) - \Psi_0 . \tag{70}$$

If x_0 and y_0 are the distances of the observer location from Ground Zero in geomagnetically eastward- and northward directions (i.e. the ground ranges), respectively,

$$\vartheta_0 = \sqrt{x_0^2 + y_0^2} \; / \; R_E \tag{71}$$

and

$$\Psi_0 = \arctan \frac{R_E \sin \vartheta_0}{H_0 + R_E (1 - \cos \vartheta_0)} . \tag{72}$$

In Section 2.2, particular use was made of Eq. (69) to calculate the angles between the line-of-sight vector and the earth magnetic field vector, whereas Eq. (67) served to evaluate the attenuation of gamma rays in a spherical atmosphere in Section 2.3.

2.8 Dipole Approximation of the Earth Magnetic Field

In the dipole approximation, the earth magnetic field at the burst point is given by its magnitude

$$|\vec{B}| = \frac{m}{(R_E + H_0)^3} \sqrt{1 + 3 \sin^2 \theta_0} \tag{73}$$

and its inclination φ_0 (dip angle)

$$\sin \varphi_0 = \frac{2 \sin \theta_0}{\sqrt{1 + 3 \sin^2 \theta_0}} \tag{74}$$

where θ_0 is the geomagnetic lattitude, and $m = 3.12 \times 10^{-5}$ Tesla x m^3 is the magnetic dipole moment. Along the line-of-sight vector between burst point and observer location, Eqs. (73) and (74) have to be modified as follows

$$B(r) = \frac{m}{(R_E + h(r))^3} \sqrt{1 + 3 \sin^2 \theta(r)} \tag{75}$$

$$\sin \varphi_0 = \frac{2 \sin \theta(r)}{\sqrt{1+3 \sin^2 \theta(r)}} \tag{76}$$

where

$$\theta(r) = \theta_0 + \vartheta(r) \frac{y_0}{\sqrt{x_0^2 + y_0^2}} = \theta_0 + \vartheta(r) \sin \varphi \tag{77}$$

and x_0, y_0 and $\vartheta(r)$ are as in Section 2.7.

2.9 Polarization

The equations of motion of the Compton electrons and the Maxwell equations were solved in Cartesian coordinates (x,y,z) as specified in Section 2.2.

Because of the transversality of the fields

$$\vec{E} = (E_x, E_y, 0) .$$

The representation of $\vec{E}$ in a local Cartesian coordinate system (x_0, y_0, z_0) attached to the observer is then obtained by the transformation

$$\begin{pmatrix} E_{x_0} \\ E_{y_0} \\ E_{z_0} \end{pmatrix} = \begin{pmatrix} -\sin\varphi & -\cos\varphi\cos\Psi & 0 \\ \cos\varphi & -\sin\varphi\cos\Psi & 0 \\ 0 & -\sin\Psi & 0 \end{pmatrix} \begin{pmatrix} E_x \\ E_y \\ 0 \end{pmatrix} \tag{78}$$

$$= \begin{pmatrix} -E_x \sin\varphi - E_y \cos\varphi\cos\Psi \\ E_x \cos\varphi - E_y \sin\varphi\cos\Psi \\ -E_y \sin\Psi \end{pmatrix}$$

where as in Section 2.2, φ is the azimuth angle of the observer location in a polar coordinate system where the pole and the polar axis coincide with Ground Zero and the eastward direction, respectively.

3. NUMERICAL RESULTS

The EXEMP code employs a fourth order Runge-Kutta algorithm to solve the equations of motion of the Compton electrons and the Maxwell equations which in the high-frequency approximation can be reduced to ordinary differential equations. If electron avalanching is taken into account, the rate equation is also solved by means of the Runge-Kutta method.

Self-consistency is achieved successively by calculating the electromagnetic fields $\vec{E}$ and $\vec{B}$ at height h over ground which are then considered as the first order external fields for the motion of the Compton electron at height h-Δh. If the spacing of height is sufficiently small ($\Delta h \leq 0{,}5$ km), no reiteration is required.

The input parameters for the subsequent numerical computations can be grouped togehter into two categories for which the following typical standard values were assumed

(I) Weapon related parameters

Gamma yield	Y_γ	= 10 kt
Height of burst	H_0	= 200 km
Gamma energy	E_γ	= 2 MeV
Rise time coefficient	α	= 1.0 ns^{-1} *)
Decay time coefficient	β	= .1 ns^{-1} *)

*QEXP gamma source function Eq. (35)

(II) Scenario and observer location dependent parameters

Geomagnetic lattitude	θ_0	= 50°
Magnitude of earth magnetic field	B_0	= 4.7×10^{-5} T
Dip angle	φ_0	= 67°
Observer location (southward of GZ)	y_0	= -2.256 H_0

The parameters of group (II) strictly speaking only apply under the assumptions of a uniform earth magnetic field over a plane earth surface. If this is not the case, θ_0, φ_0 and B_0 vary along the line-of-sight between detonation point and observer, as shown in Section 2.8.

For the specified observer location, the line-of-sight vector ist perpendicular to the earth magnetic field. Hence the maximum electric peak field strength could be expected in this case (However the actual numerical calculations indicate that the maximum values are reached at $y_0 \approx -1.5\ H_0$).

In each of the Figs. 1 to 5 only one parameter of category (I) was varied keeping all the other parameters of categories (I) and (II) unchanged.

In particular, in Fig. 1 higher yields produce fields with faster rise time and smaller half-width. The peak values saturate at 50 kV/m for gamma yields > 10 kt. For low yields, the peak field strength is proportional to the yield.

Fig. 2 depicts the dependency on the height of burst. The maximum peak values are obtained for bursts in the region H_0 = 100 to 200 km. Higher HOBs tend to increase rise time and pulse width.

Fig. 3 shows the electric field as a function of the gamma energy. The peak field saturates at 50 kV/m for $E_\gamma > 2$ MeV.

The dependency on various spectral distributions is investigated in Fig. 3a. The gamma leakage spectrum is as calculated by H.A. Sandmeier et al. [8] for a 24 kt high-leakage fission weapon, however scaled to a gamma yield of 10 kt. Very little difference in the corresponding EMP is observed on replacement of the leakage spectrum by the original Plutonium fission spectrum. The curve for E_γ= 1.3 MeV corresponds to the average energy of the fission spectrum.

The influence of various rise times $1/\alpha$ of the gamma source function is investigated in Fig. 4. As expected, this variation is reflected in the EMP rise time. The peak electric field is slightly increasing with the rise time.

The effect of the gamma pulse decay time variation is studied in Fig. 5. (In this particular diagram, zero rise time, i.e. $\alpha \rightarrow \infty$, was chosen in order to compare with CHAP results and the delta function as the limiting case). Variations of decay times influence only the first 10 ns of the EMP. After this the decay of the electric field is mostly governed by the turning of the Compton electrons in the earth magnetic field and their energy loss due to ionization.

Figs. 6 to 8 are devoted to the influence of various approximations and/or improvements. Again, these results are obtained for the standard input parameters as quantified above, and under the assumption of uniform earth magnetic field and plane earth surface.

Fig. 6 shows EMP fields at two different observer locations calculated with and without consideration of self-consistency. The main difference between the two EXEMP versions is computation time. Whereas CPU time increases proportional to the square N^2 of the number of time bins in the first case, it goes only like N in the second. Nevertheless, all calculations presented in this paper were performed self-consistently.

Fig. 7 additionally illustrates the influence of avalanching (which is almost negligible on the earth) and of secondary ionization time lag. The influence of these effects is of different significance at different observer locations.

Fig. 8 shows that above 30 km the role of avalanching can be very important because of the substantial conductivity build-up at times > 10 ns.

All subsequent calculations deal with the dependency of the EMP on the observer location relative to Ground Zero with the improvement of a dipole earth magnetic field and a spherical earth surface and atmosphere.

Figs. 9 to 11 present EMP fields northward, southward and in east-west direction with respect to Ground Zero for several observer locations denoted by (x_0, y_0). For H_0 = 200 km, the explosion horizon is at a distance of 7.87 H_0 = 1575 km from GZ. The peak electric fields are only one half of

the maximum peak electric fields to be expected around (0, - 1.5 H_0), however the pulse duration is considerably longer.

Fig. 12 and 13 summarize the peak electric fields in north-south and east-west directi respectively, including the corresponding electric field components E_{xo}, E_{yo}, E_{zo} in an observer-centered Cartesian coordinate system as determined in Section 2.9.

Fig. 14 shows the corresponding pulse half-width, numerical values of the energy density can be obtained from Fig. 15. From this it is estimated that 1 % of the original gamma yield of 10 kt is transferred to electromagnetic field energy received on the earth surface.

Fig. 16 and 17 present contour plots of the peak values of the electric field magnitude E and the vertical component E_{zo}.

Fig. 18 is a plot of the horizontal electric field vector (E_{xo}, E_{yo}).

Figs. 19 to 21 show the variation of EMP with Ground Zero at different geomagnetic latitudes. For each latitude, the electric field was calculated for the three distinguished observer location with respect to Ground Zero. In Fig. 19 the electric fields are investigated at Ground Zero, in Fig. 20 at the explosion horizon. Fig. 21 shows the pulses at the observer location $x_0=0$, $y_0<0$ where the highest peak electric fields are expected. In Figs. 20 and 21 the electric fields increase with increasing geomagnetic latitude, in Fig. 19 the opposite behavior is observed. In Figs. 19 and 20, this fact is explained by the respective angle between the incident gamma ray and the local earth magnetic field vector. In Fig. 21 the observer locations are such that the line-of-sight vector is essentially perpendicular to the local earth magnetic field in the gamma deposition layer. However, for the vertical incidence near the equator where the magnetic field is parallel to the earth surfac the maximum of gamma energy deposition occurs at lower heights than for the grazing incidenc for higher latitudes where the gamma rays have to travel longer optical distances in the atmosphere. Hence, at the equator saturation occurs at earlier times than in polar regions.

A comparison of EXEMP and CHAP results is shown in Fig. 22 for three selected observer locations.

In view of the discussion of new EMP standards, a few calculations under 'worst-case' assumptions were performed. Since the rise time ΔT (10-90 %) of the EMP tends to decrease with decreasing HOB, a height of burst of 120 km was combined with a gamma source of 10 kt (corresponding to a nuclear weapon in the high megaton range) and infinitely short rise-time (i.e. Longmire's decaying step function) of the gamma pulse.

Fig. 23 shows higher peak fields and shorter rise times (E_{peak}= 70 kV/m, ΔT(10-90 %) ≈ 1 ns) then in the previous diagrams. However, for more realistic rise-times of the gamma source (α = 1.0/ns) the corresponding EMP rise-time can hardly fall below 3 ns.

In Fig. 24 even higher peak electric fields of more than 100 kV/m are obtained when the gamma energy increases from E_γ = 2 MeV (as in Fig. 23) to a (perhaps unrealistic) value of 4 MeV. This indicates that for a lower HOB the gamma energy for which saturation of the electric fields occurs

is shifted to higher values than in Fig. 3. An obvious explanation is that because of the shorter rise - time the build-up of ionization still lags behind its saturation while the Compton current already reaches its maximum.

It is again demonstrated by Figs. 23 and 24 that a combination of the maximum peak fields (obtained at $y_0 \approx -250$ km), shortest rise-times and longest pulse durations (obtained at explosion horizon) never occurs at the same location in a single detonation. If despite of this fact both quantities are combined in a single worst-case pulse (e.g. for standardization of testing equipment) one should be aware that the energy density can be overestimated by an order of magnitude.

REFERENCES

1. C.L. Longmire, R.M. Hamilton, and J.M. Hahn, A Nominal Set of High-Altitude EMP Environments, Theoretical Notes TN 354, 1987.

2. W.J. Karzas and R. Latter, Detection of the Electromagnetic Radiation from Nuclear Explosions in Space, Phys. Rev., Vol. 137, 5B, p. 1369, 1965

3. C.L. Longmire, On the Electromagnetic Pulse Produced by Nuclear Explosions, IEEE Trans. on Ant. and Prop., Vol. AP-26, No. 1, p. 3, 1978

4. C.L. Longmire and H.J. Longley, Improvements in the Treatment of Compton Current and Air Conductivity in EMP Problems, DNA 3192T, 1973

5. R.D. Evans, Compton Effect, Handbuch der Physik (S. Flügge, ed.), Vol. XXXIV, p. 218, 1958

6. C.N. Vittitoe, Electron Attachment and Avalanching Associated with EM Calculations for High-Altitude Bursts, SLA-73-0494, 1973

7. D.K. Davies, Measurement of Swarm Parameters in Dry Air, Theoretical Notes TN 346, 1983

8. H.A. Sandmeier, S.A. Dupree and G.E. Hansen, Electromagnetic Pulse and Time-Dependent Escape of Neutrons and Gamma Rays from a Nuclear Explosion, Nucl. Sci. and Eng., Vol. 48, p. 343, 1972.

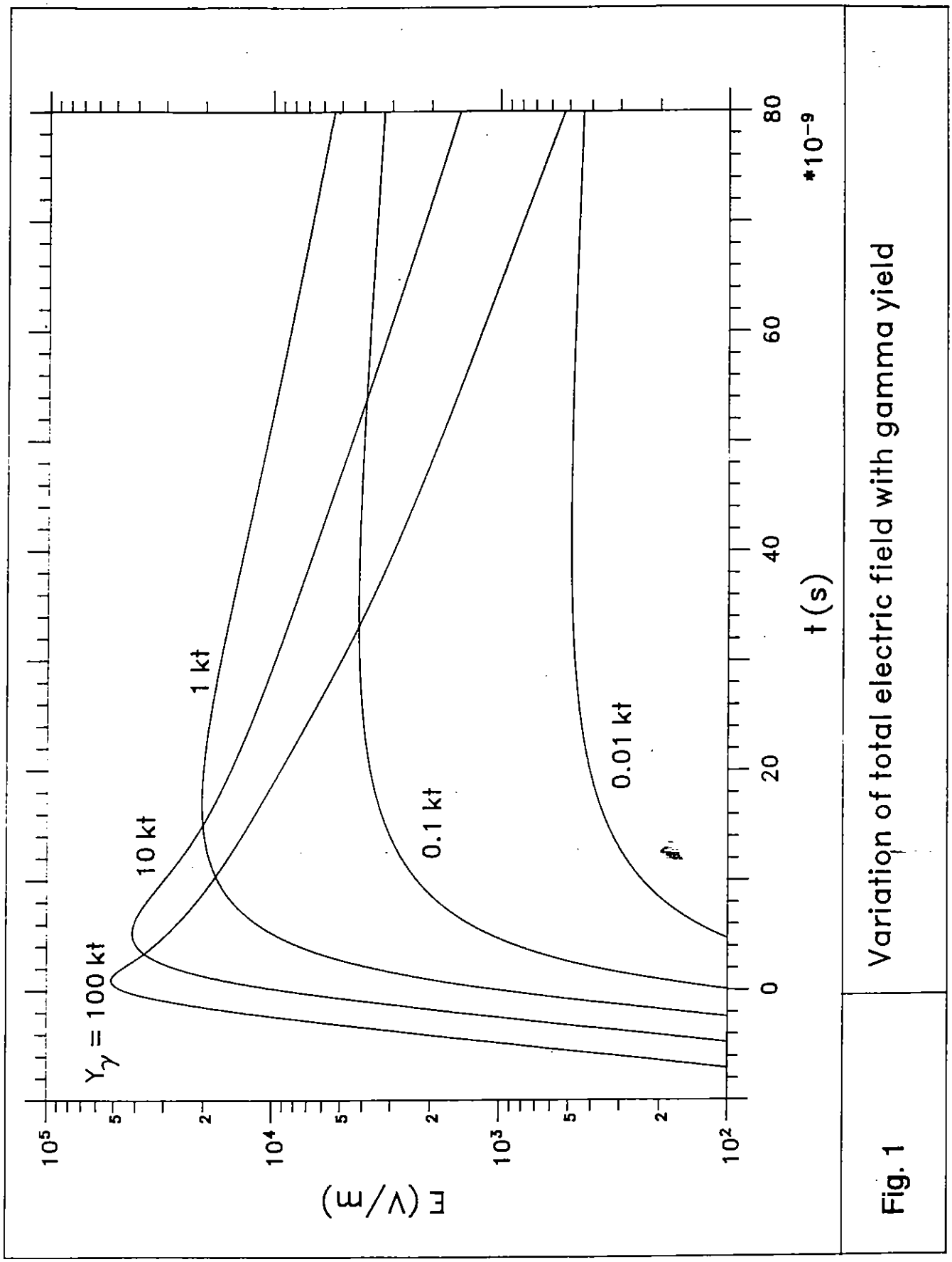

Fig. 1 Variation of total electric field with gamma yield

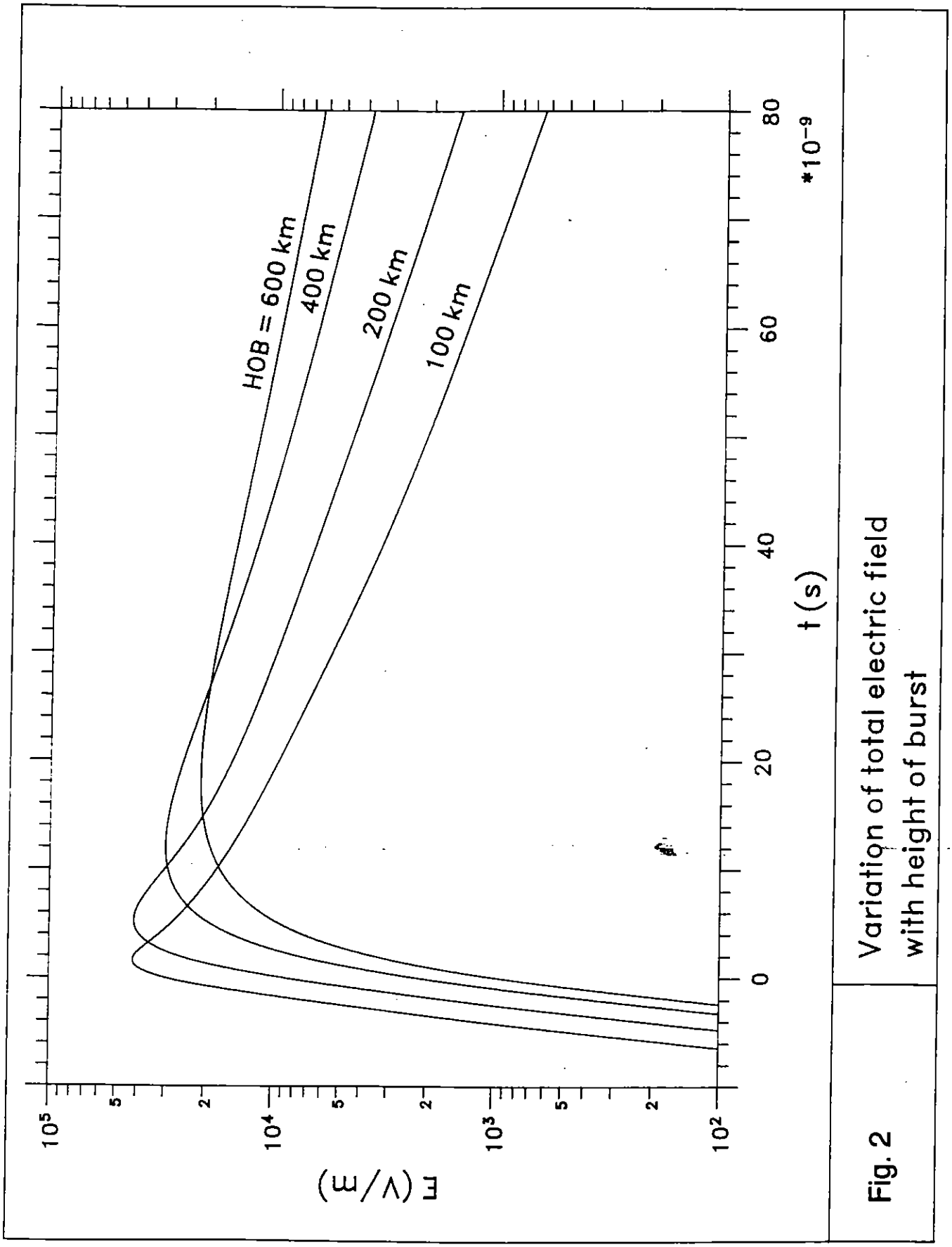

Fig. 2 Variation of total electric field with height of burst

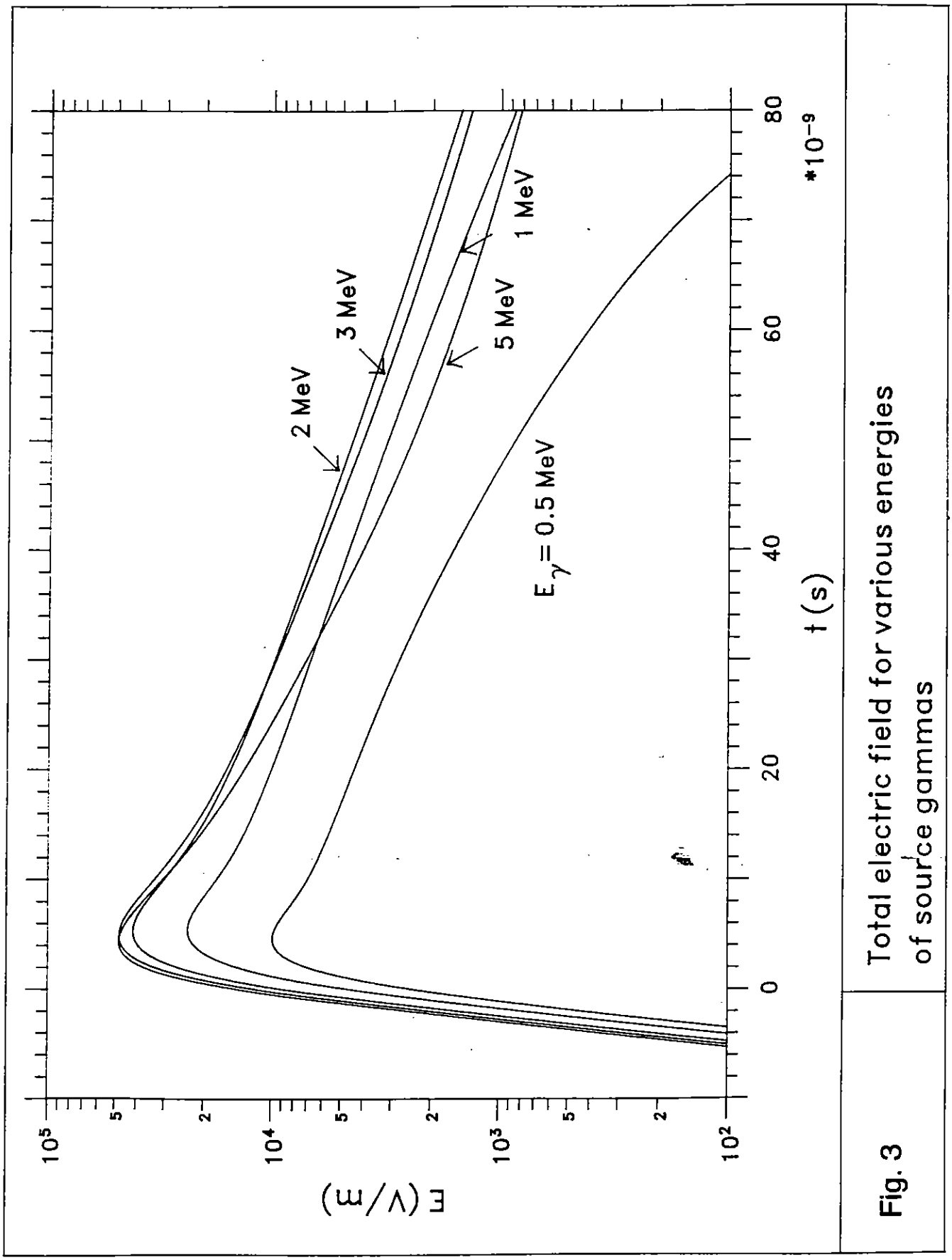

Fig. 3 Total electric field for various energies of source gammas

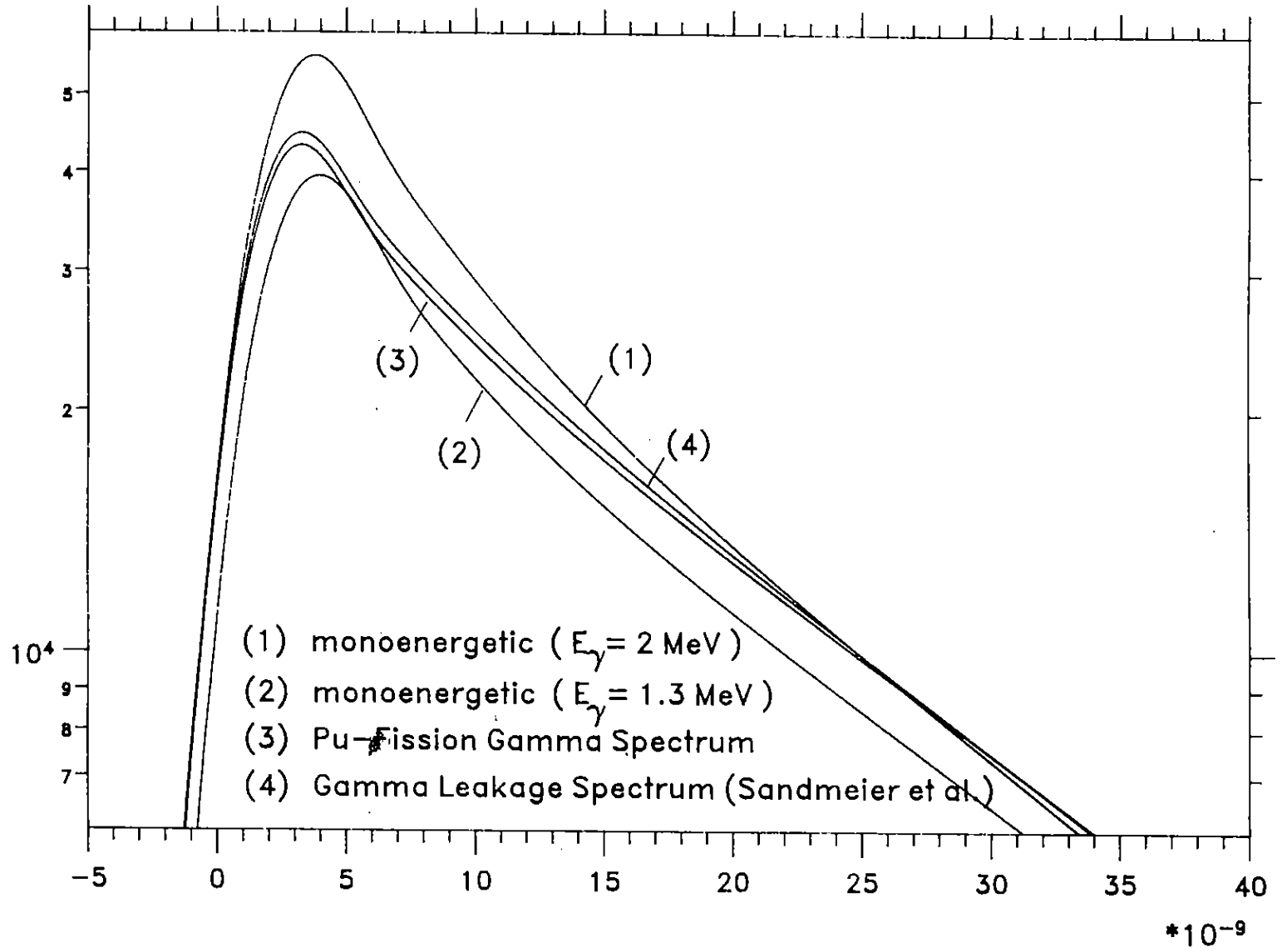

Fig. 3a

Electromagnetic pulse shapes for different gamma spectra

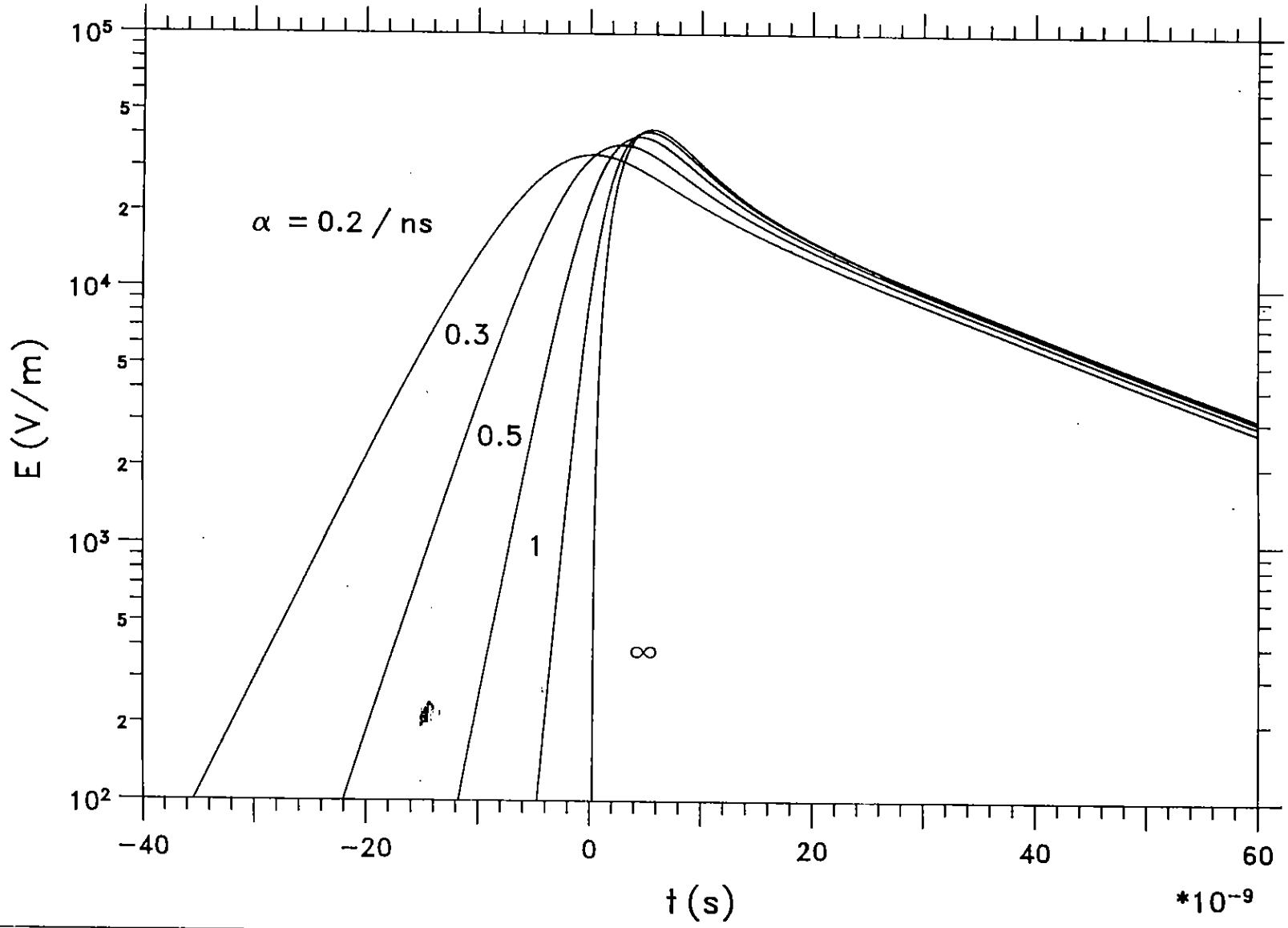

Fig. 4

Total electric field (field magnitude) for various gamma pulse rise times 1/Alpha

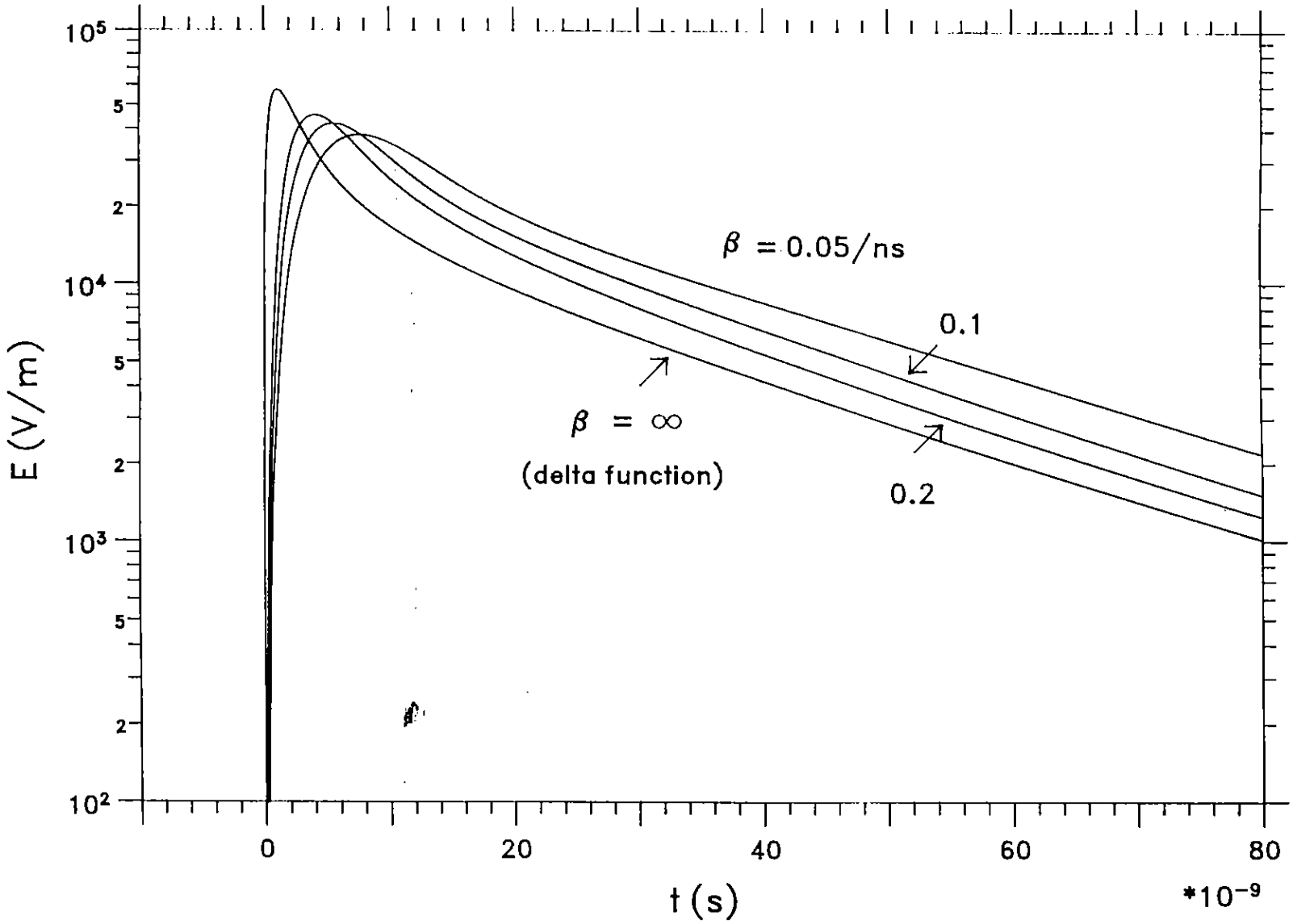

Fig. 5	Total electric field for various gamma pulse decay times 1/Beta

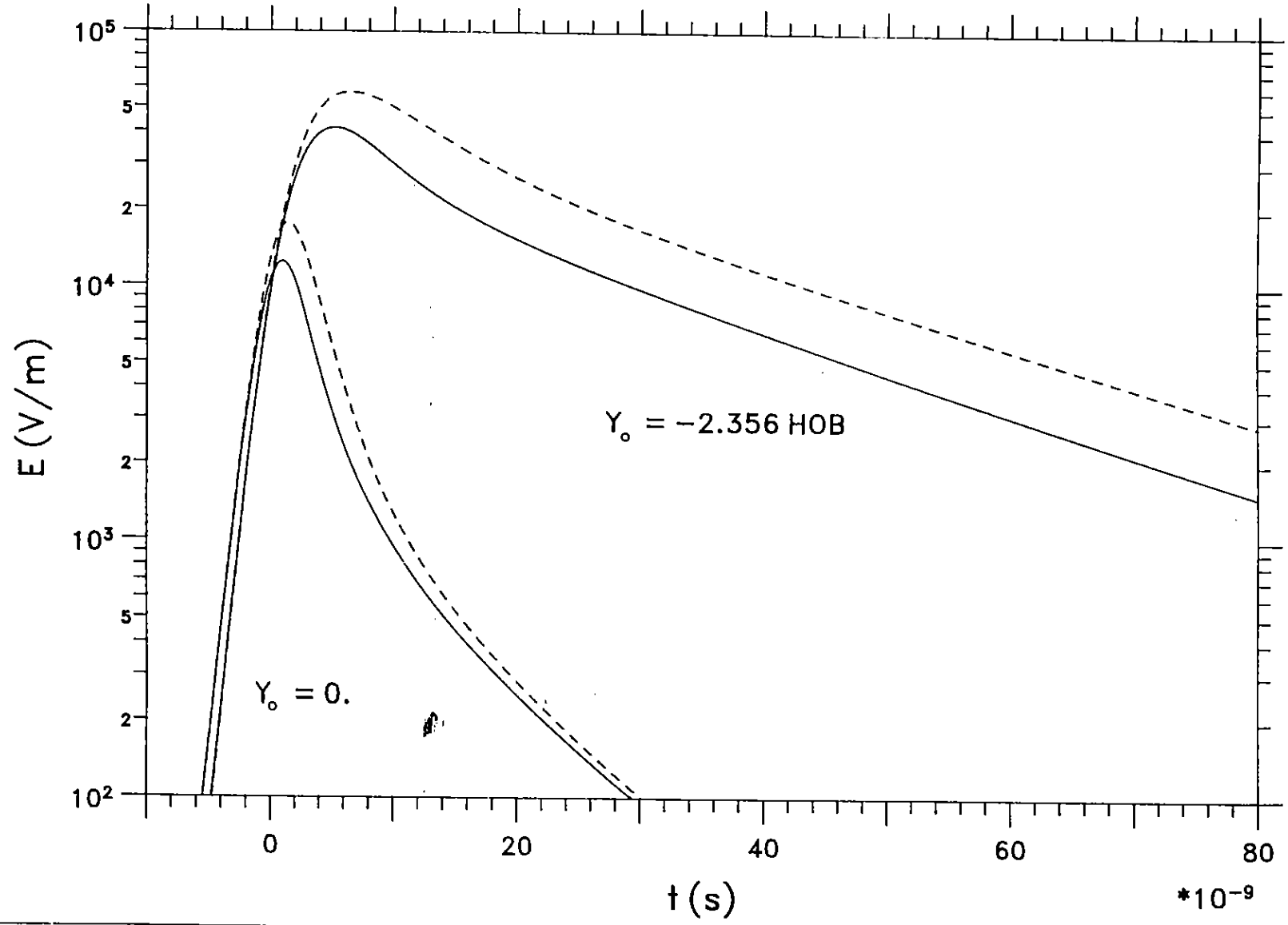

Fig. 6	Comparison of self−consistent and non−self−consistent solutions (−−−)

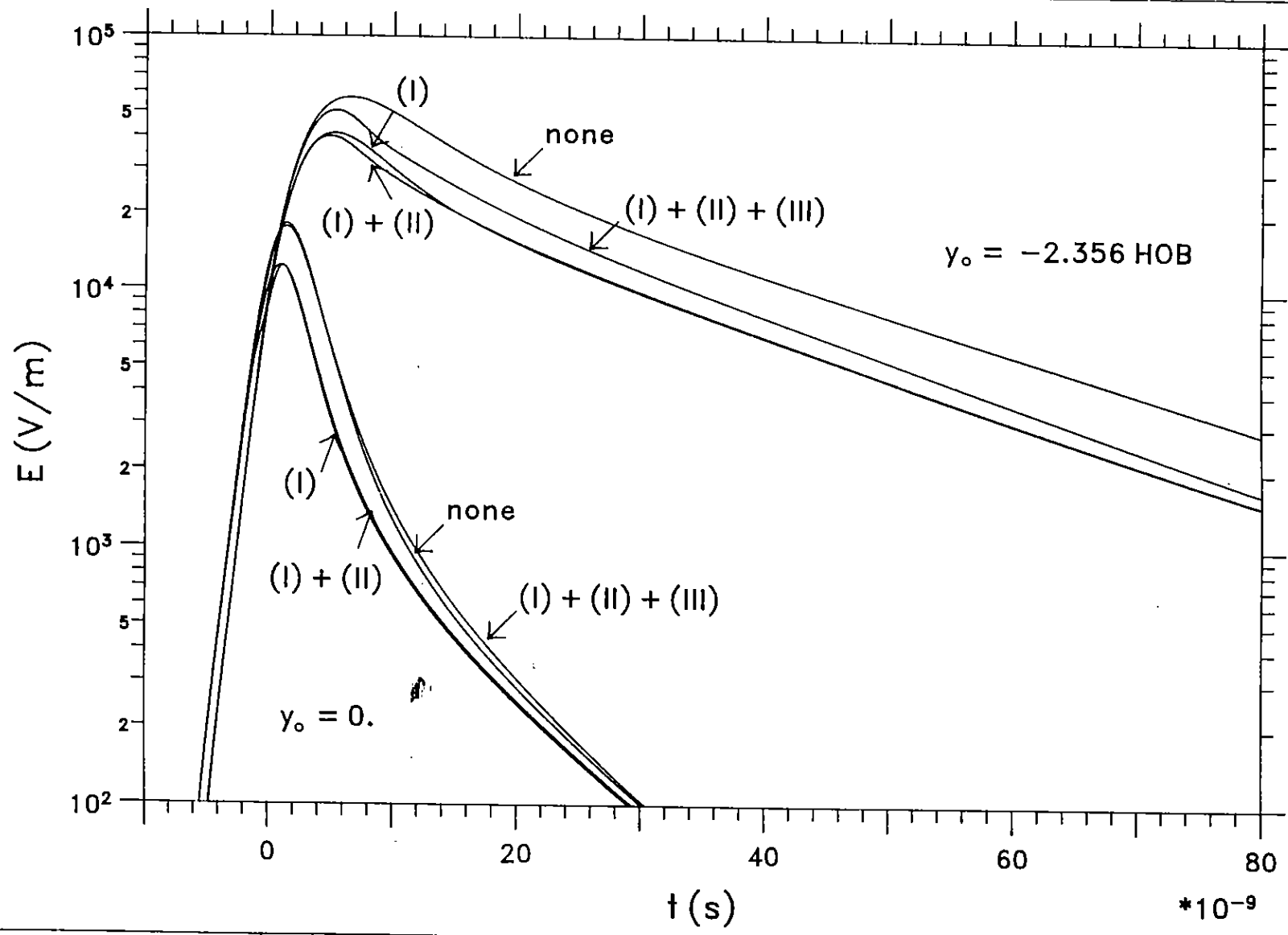

Fig. 7

Influence of the effects of self−consistency (I), avalanching (II) and secondary ionization time lag (III)

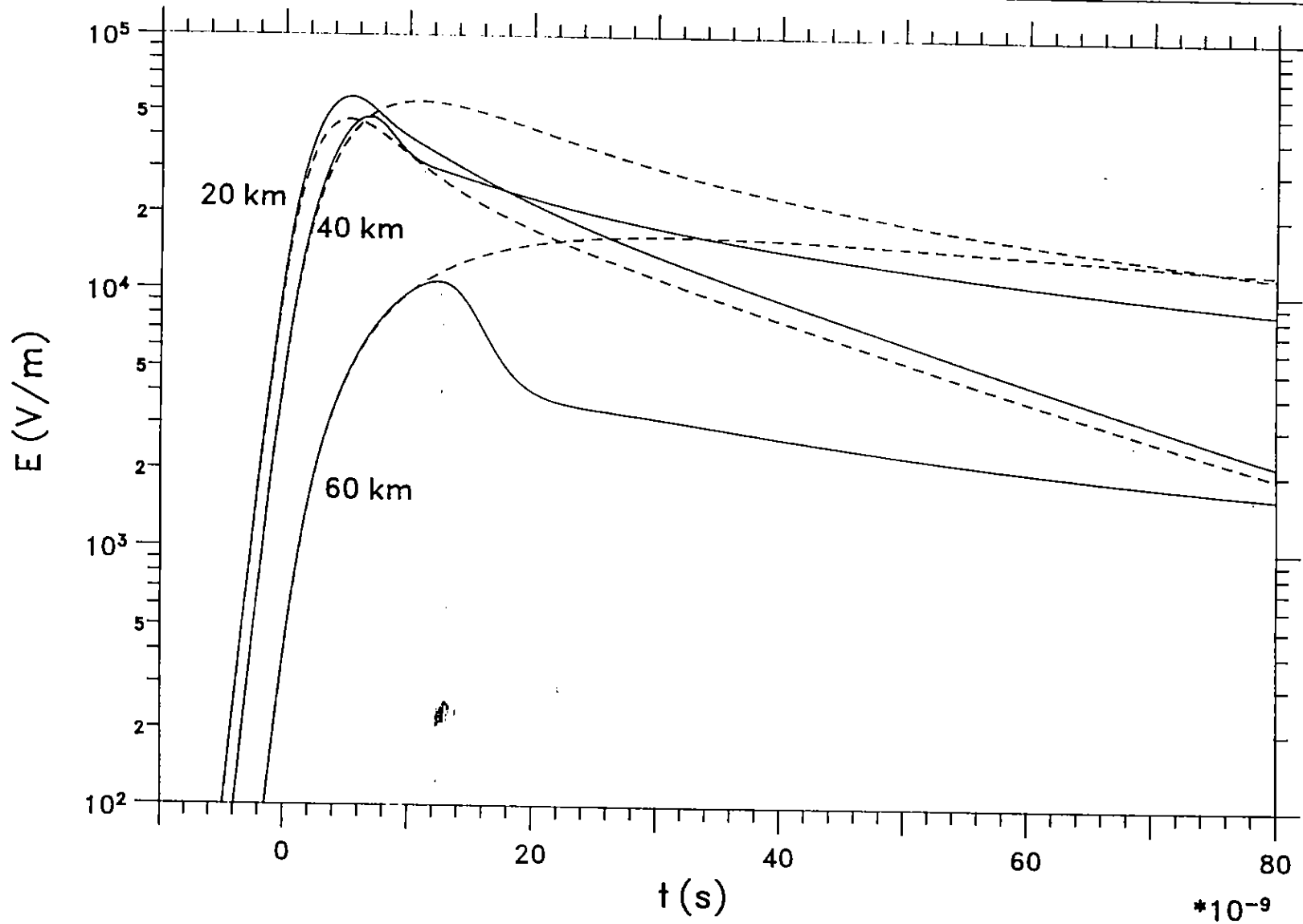

Fig. 8	Total electric fields in various heights neglecting (– – –) and including the effects of avalanching and ionization time lag

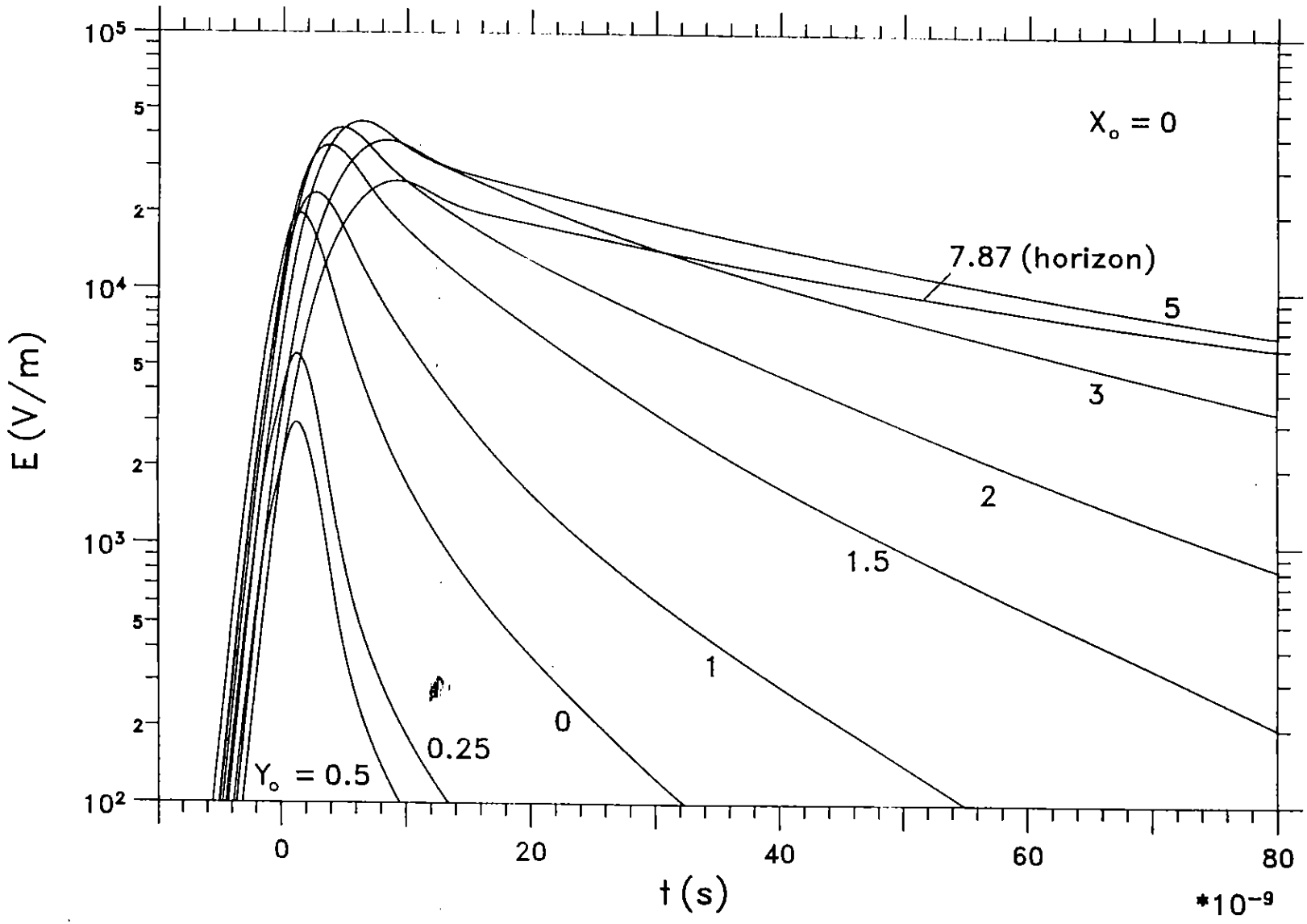

Fig. 9

Total electric fields at various observer locations north of Ground Zero (in units of HOB = 200 km)

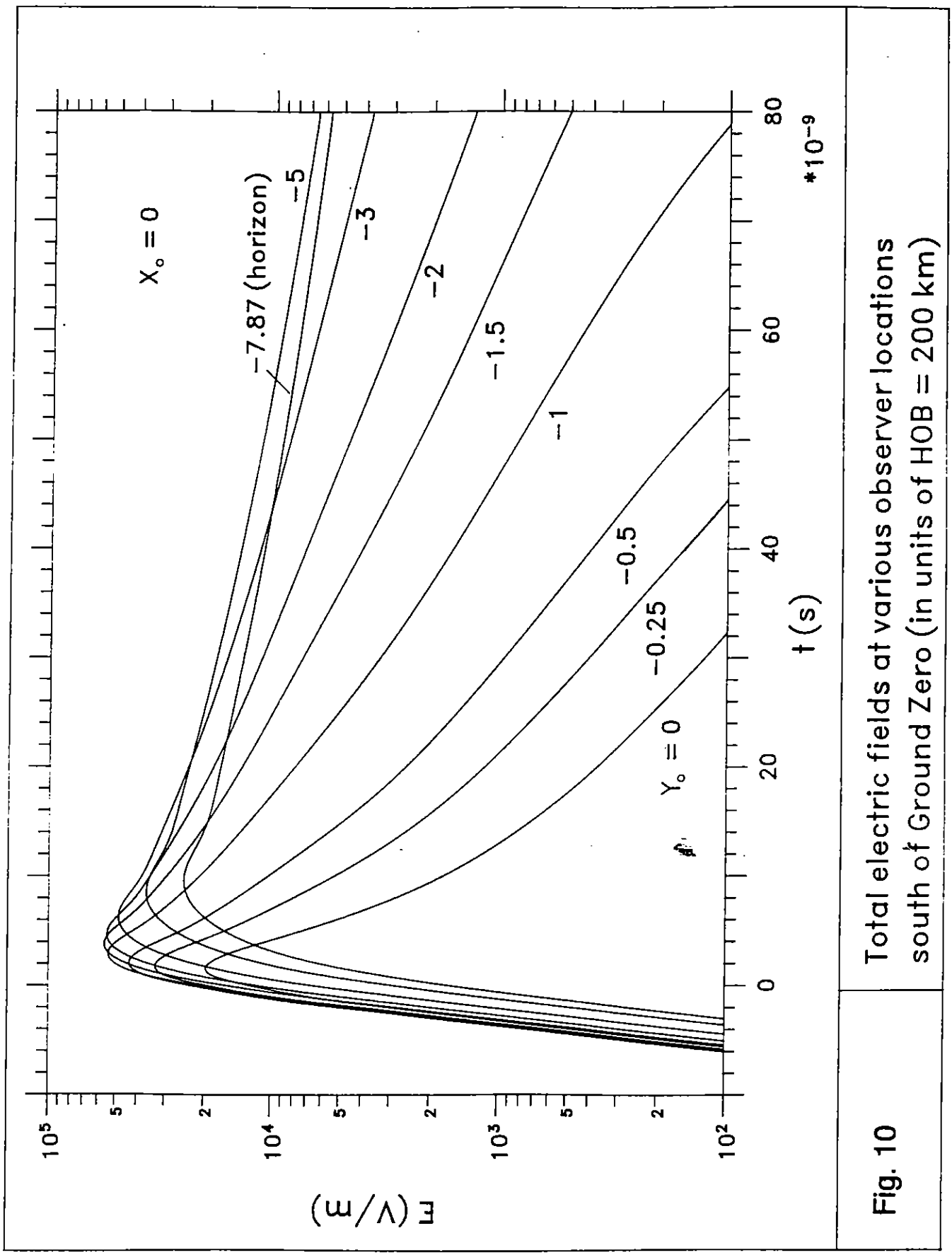

Fig. 10 Total electric fields at various observer locations south of Ground Zero (in units of HOB = 200 km)

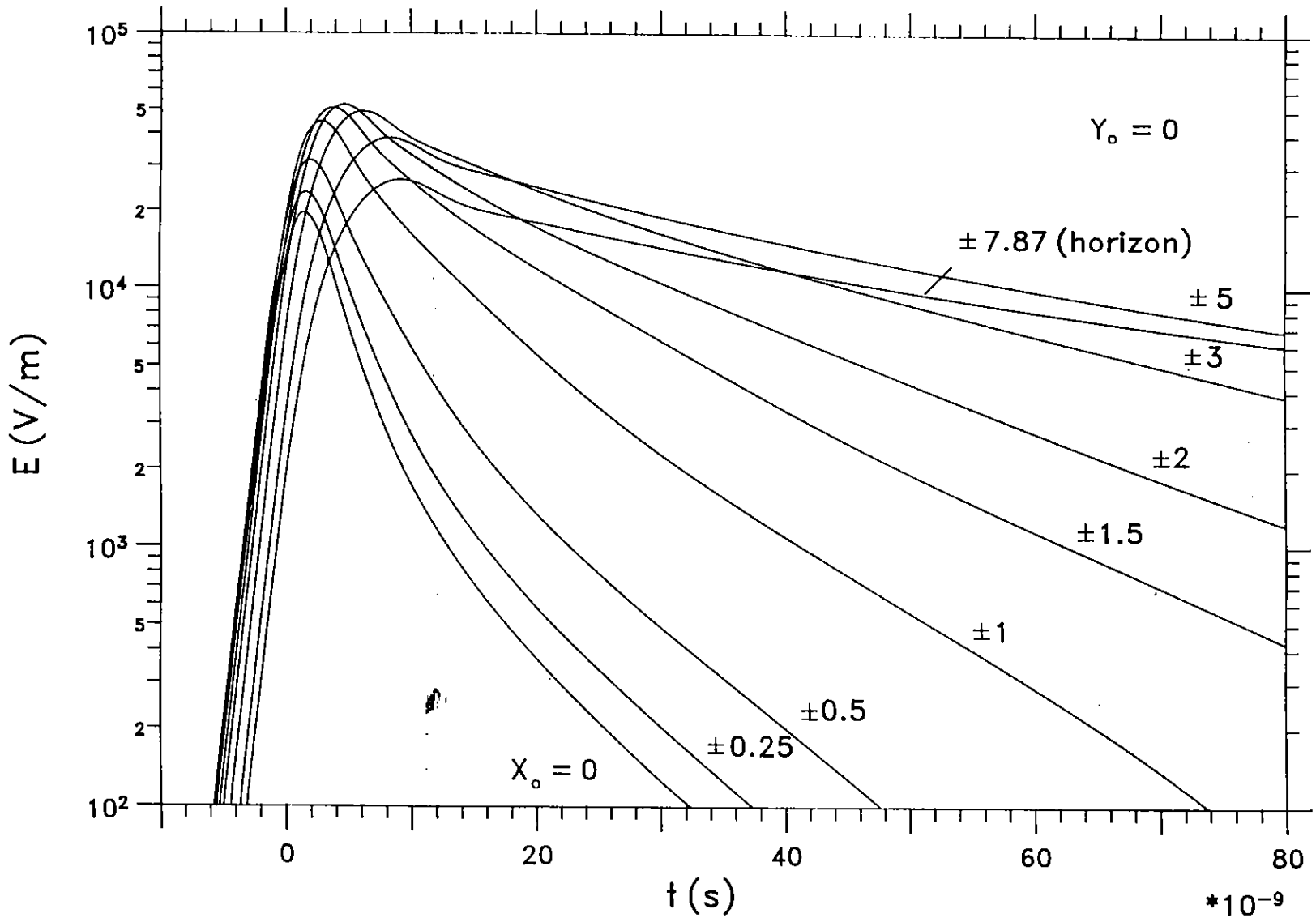

Fig. 11	Total electric field at various locations east and/or west of Ground Zero (in units of HOB = 200 km)

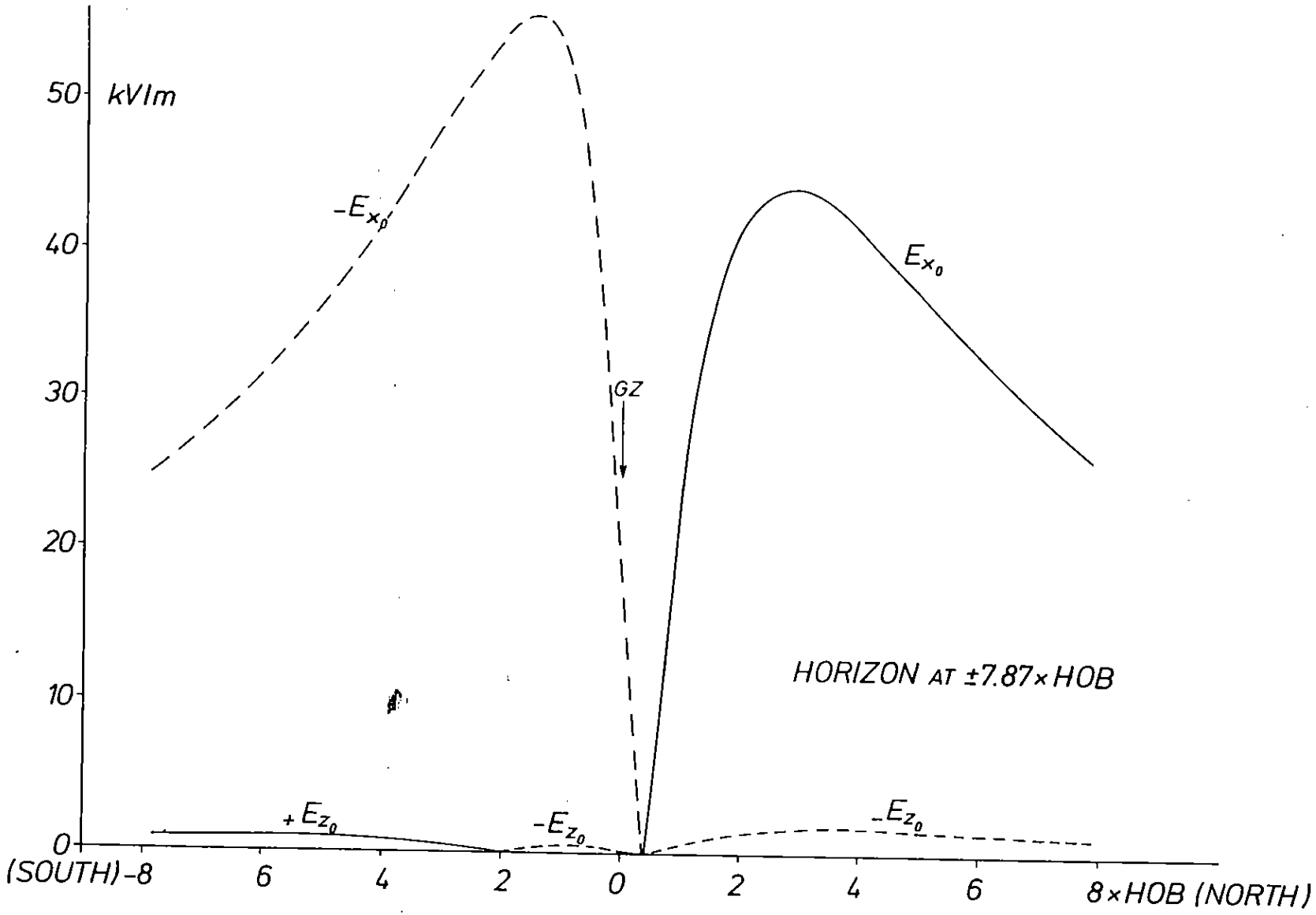

Fig. 12. Components of the peak electric field vector along the geomagnetic meridian through GZ in observer-centered Cartesian coordinates.

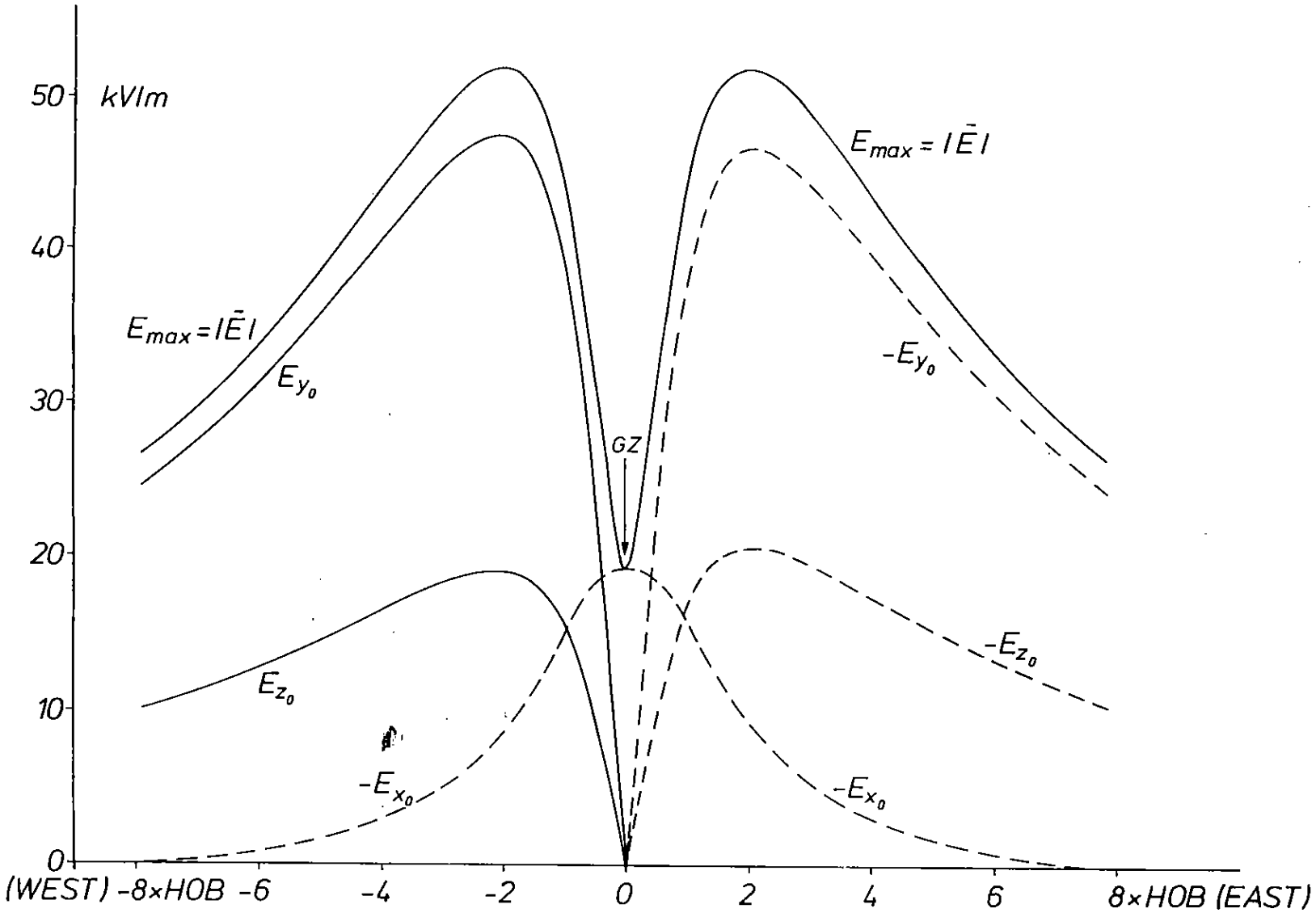

Fig. 13. Components of the peak electric field vector along the geomagnetic parallel of latitude through GZ in observer-centered Cartesian coordinates.

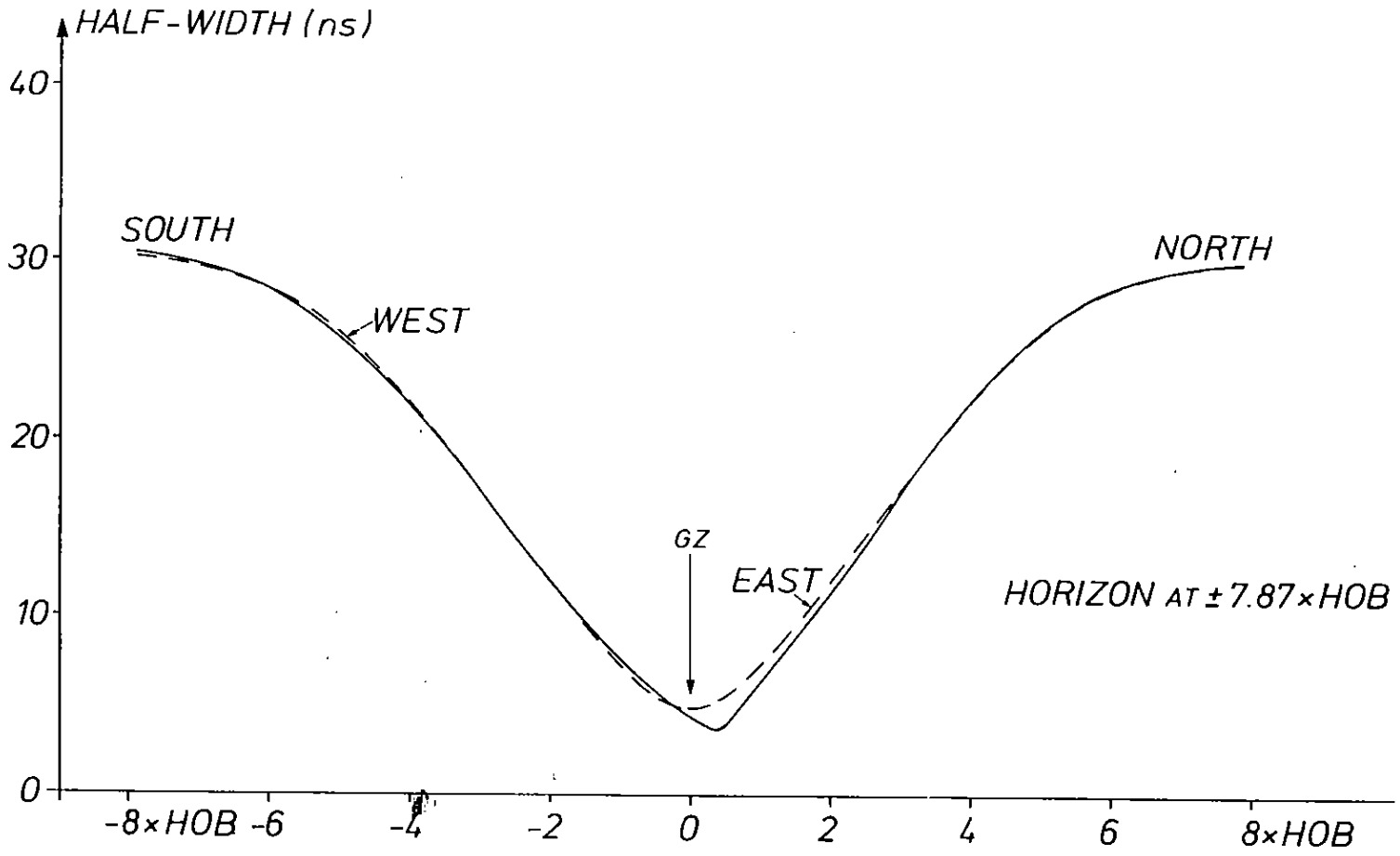

Fig. 14. Pulse half-widths of the pulses received by observers along the parallel and meridian through GZ.

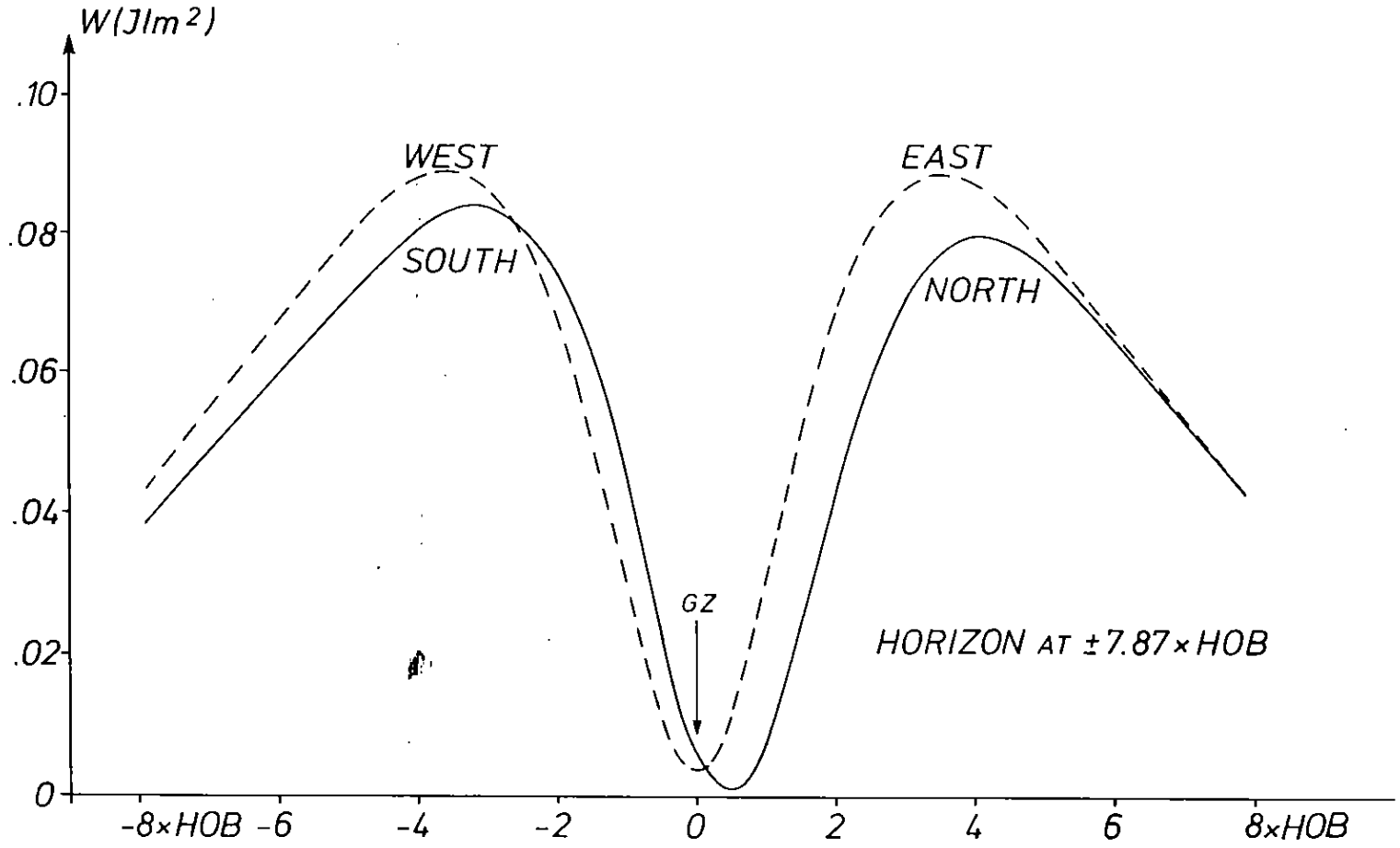

Fig. 15. Energy densities along the parallel and meridian through GZ.

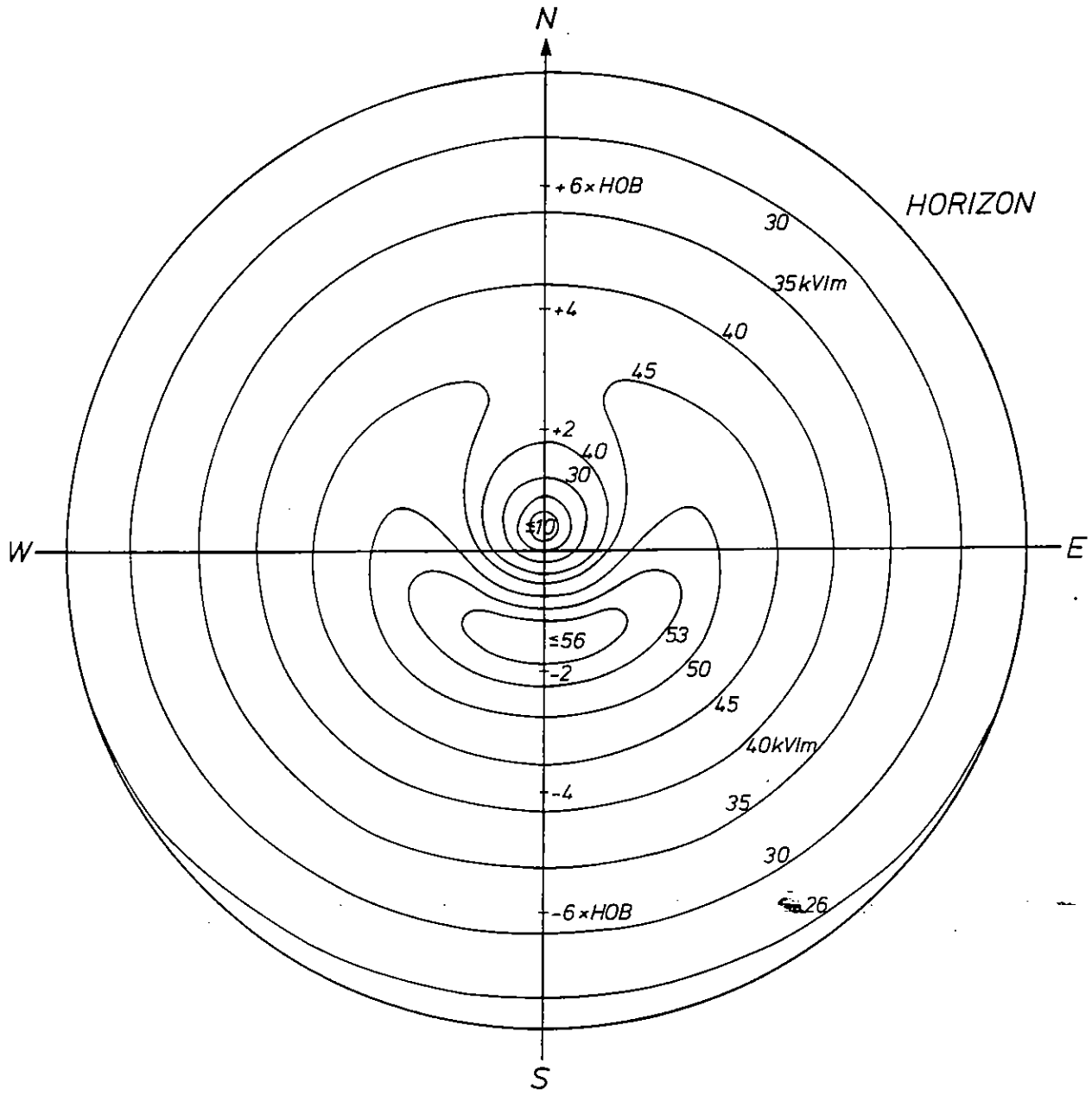

Fig. 16. Contour plot of peak electric field magnitudes.

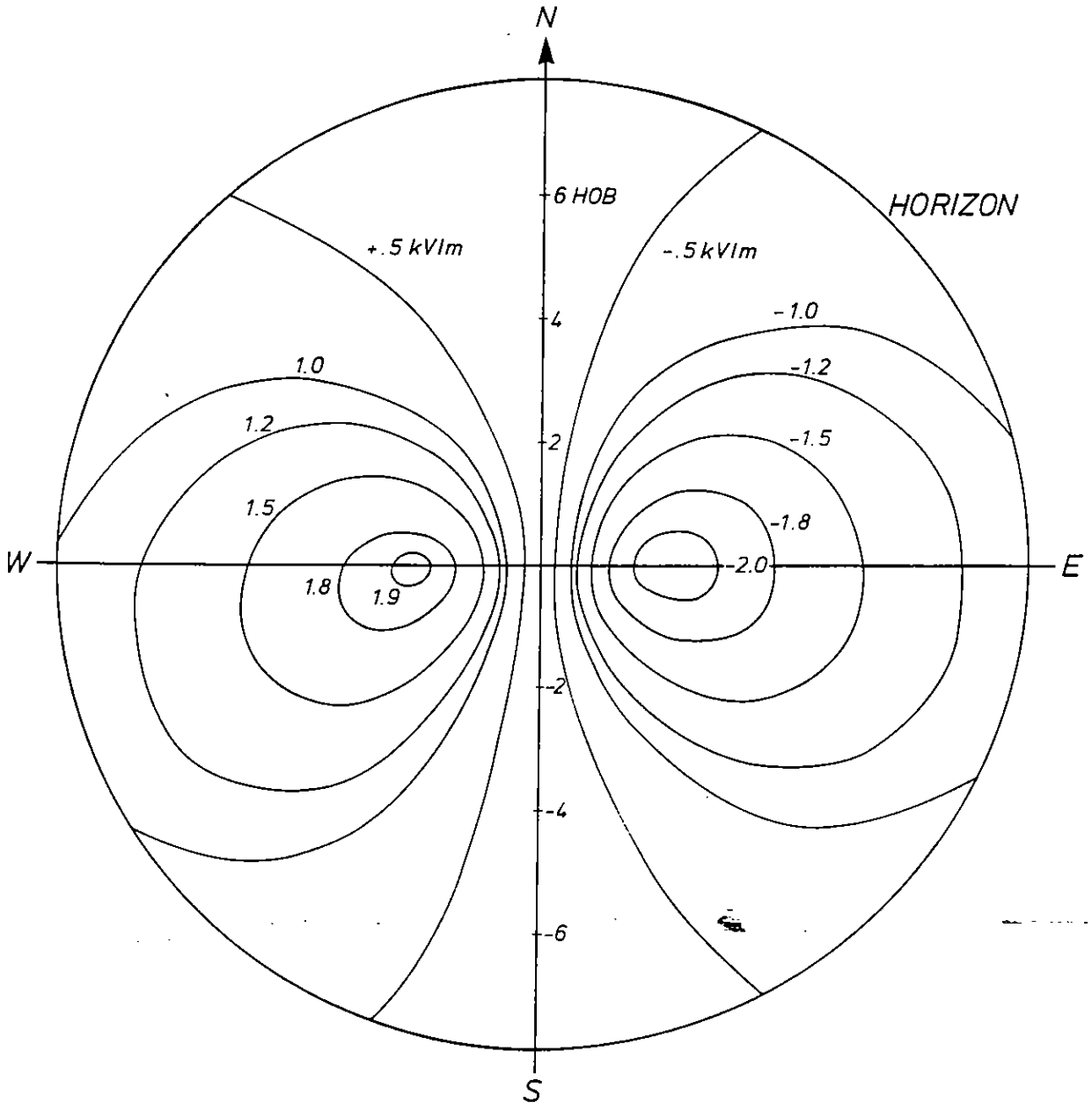

Fig. 17. Contour plot of the vertical electric field component.

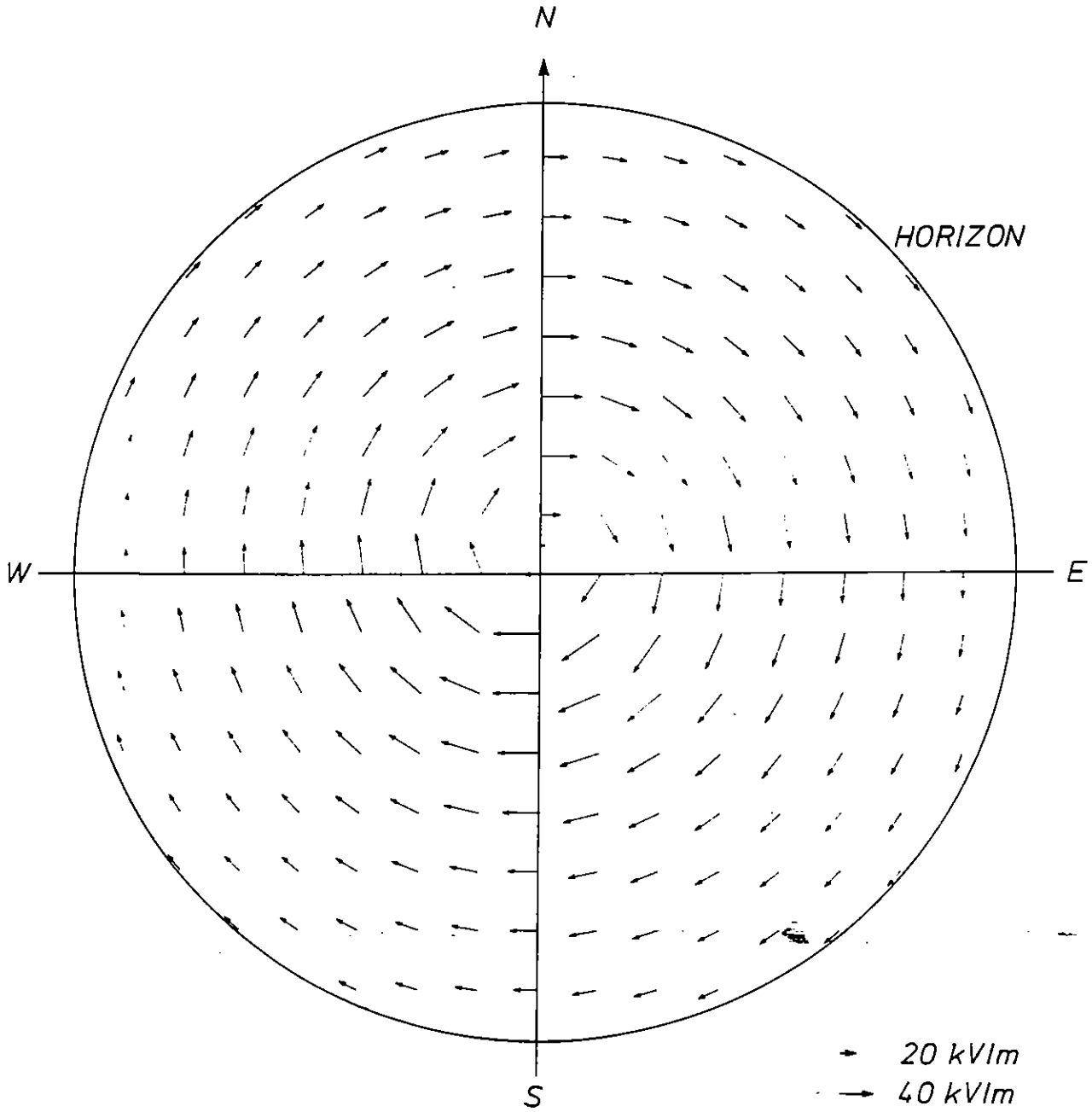

Fig. 18. Horizontal electric field vectors.

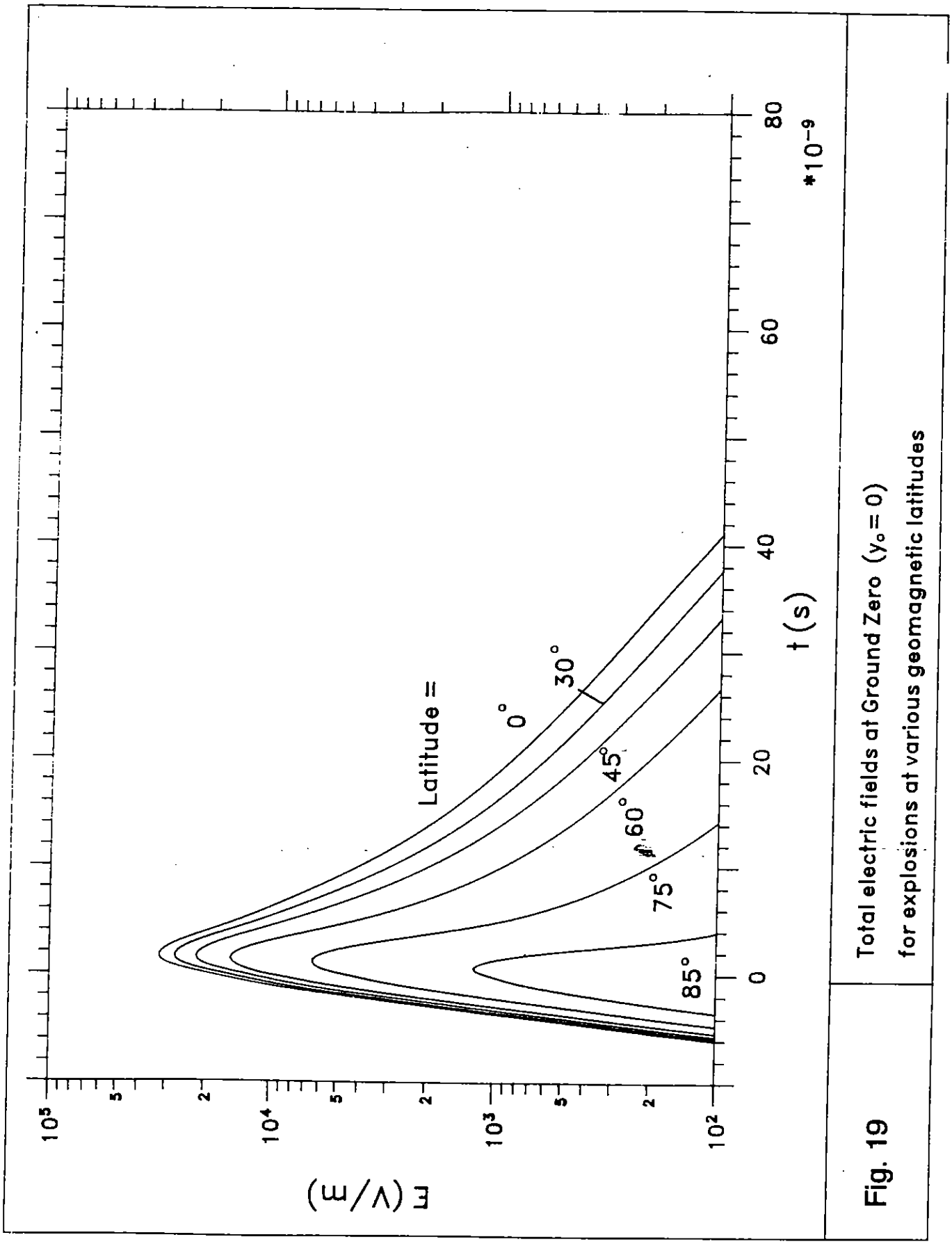

Fig. 19

Total electric fields at Ground Zero ($y_o = 0$)
for explosions at various geomagnetic latitudes

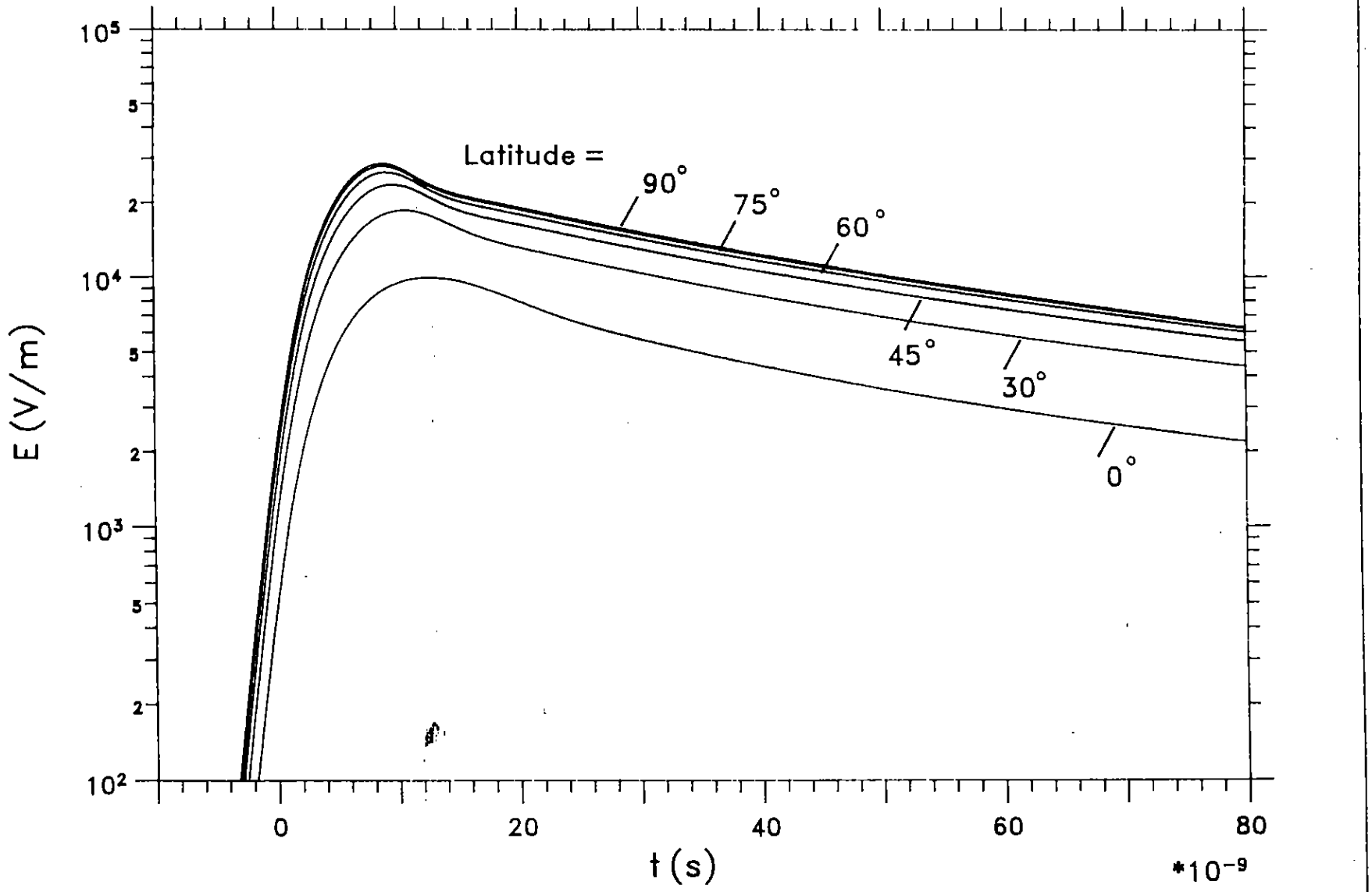

Fig. 20	Total electric fields at explosion horizon (y_o = −7.87, ground range = 1570 km) for explosions at various geomagnetic latitudes

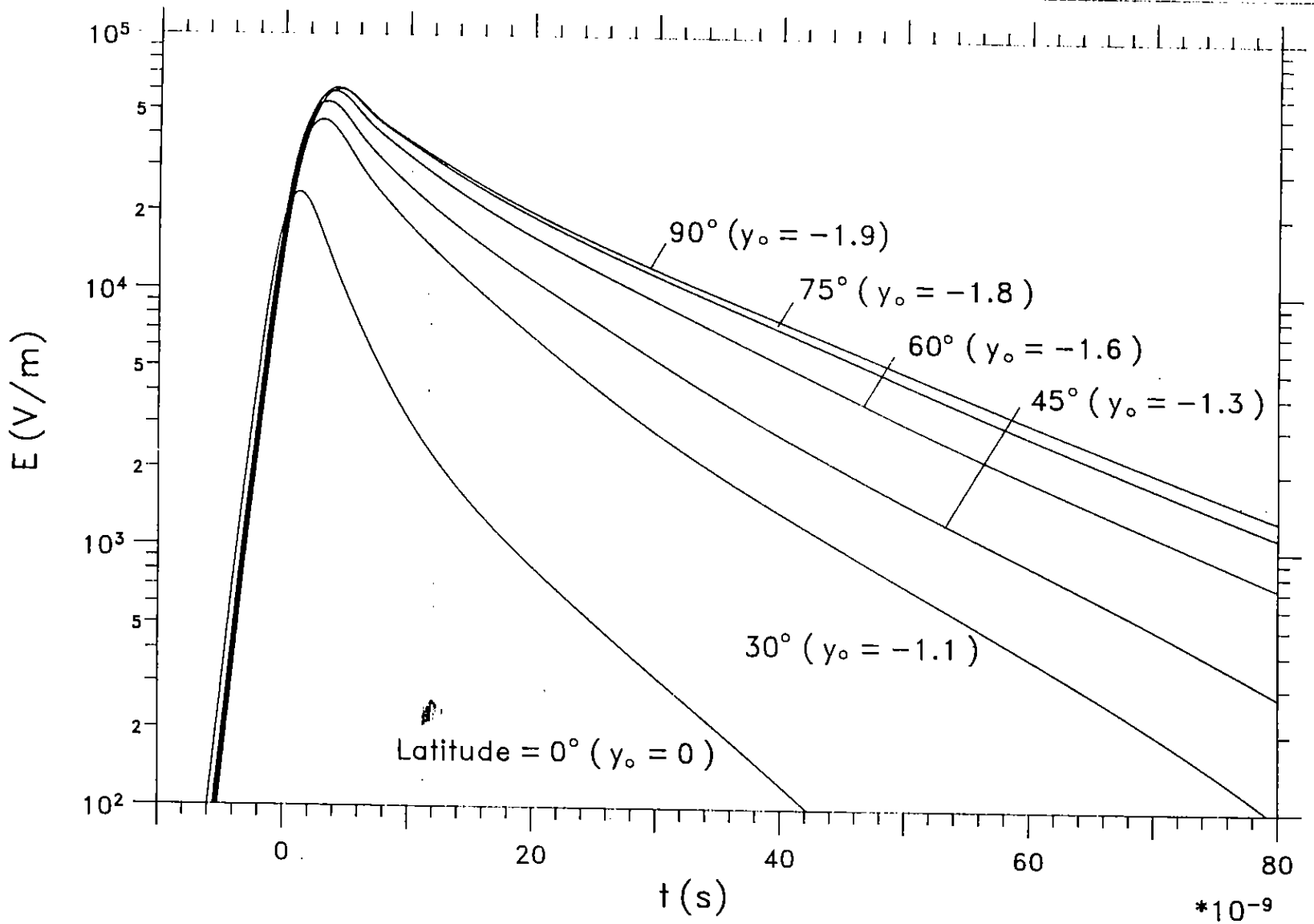

Fig. 21 Maximum total electric fields at observer location y_o (in units of HOB = 200km, southward of GZ) for explosions at various geomagnetic latitudes

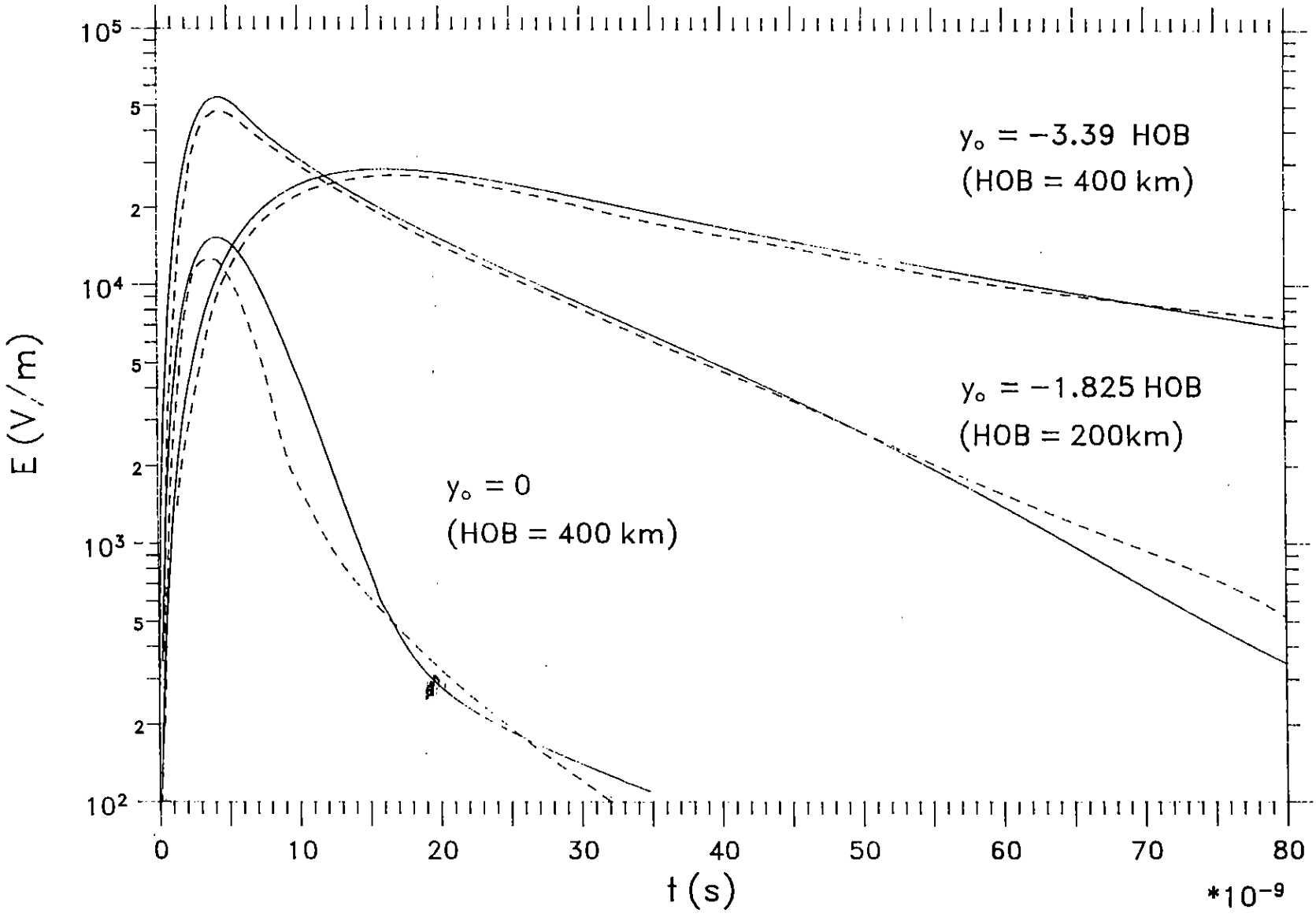

Fig. 22 Comparison with CHAP results (– – –) at various observer locations ($x_o = 0, y_o$)

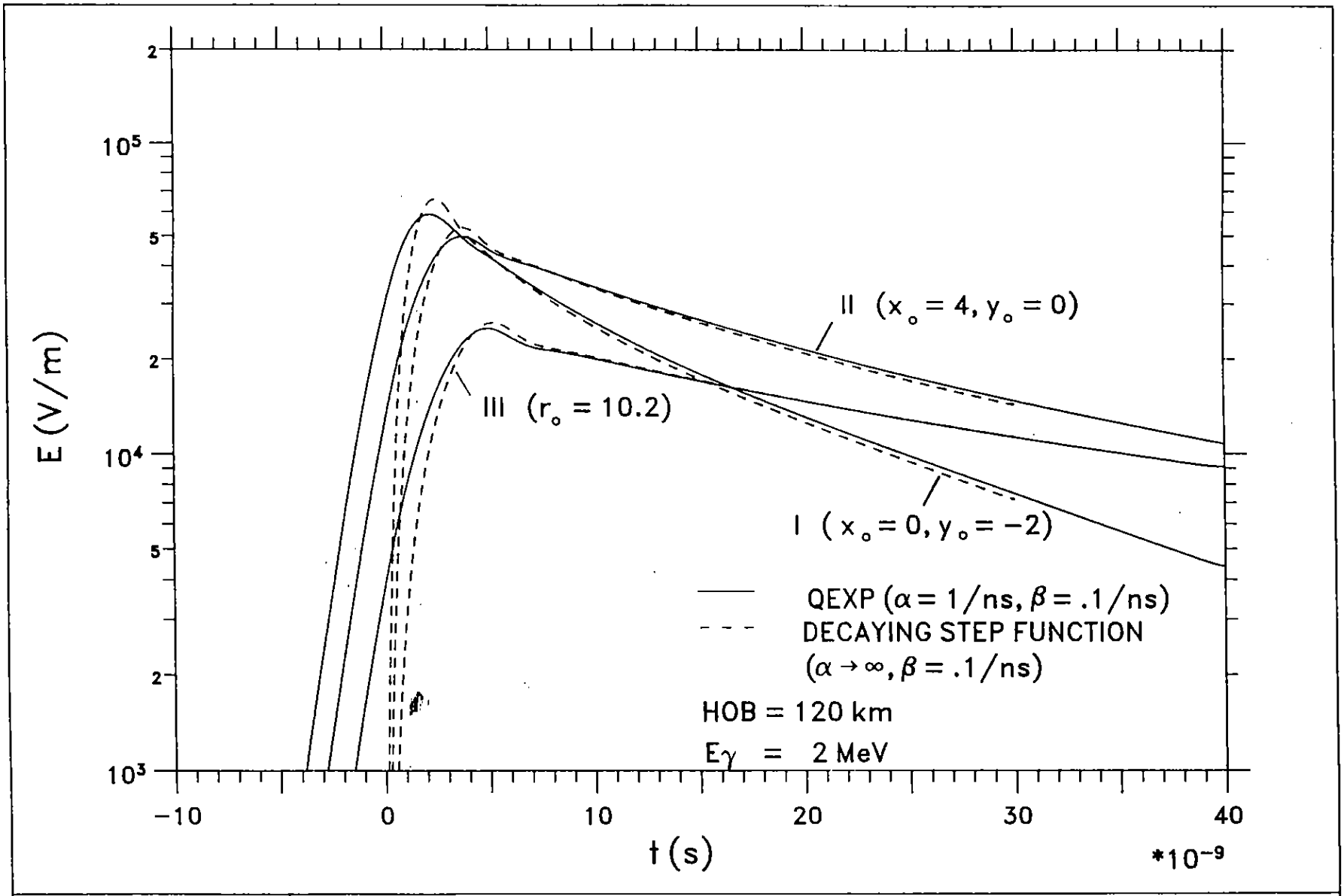

Fig. 23

Total electric fields at 3 different observer locations: (I) maximum peak field, (II) max energy density of .08 J/m^2, (III) explosion horizon (in units of HOB)

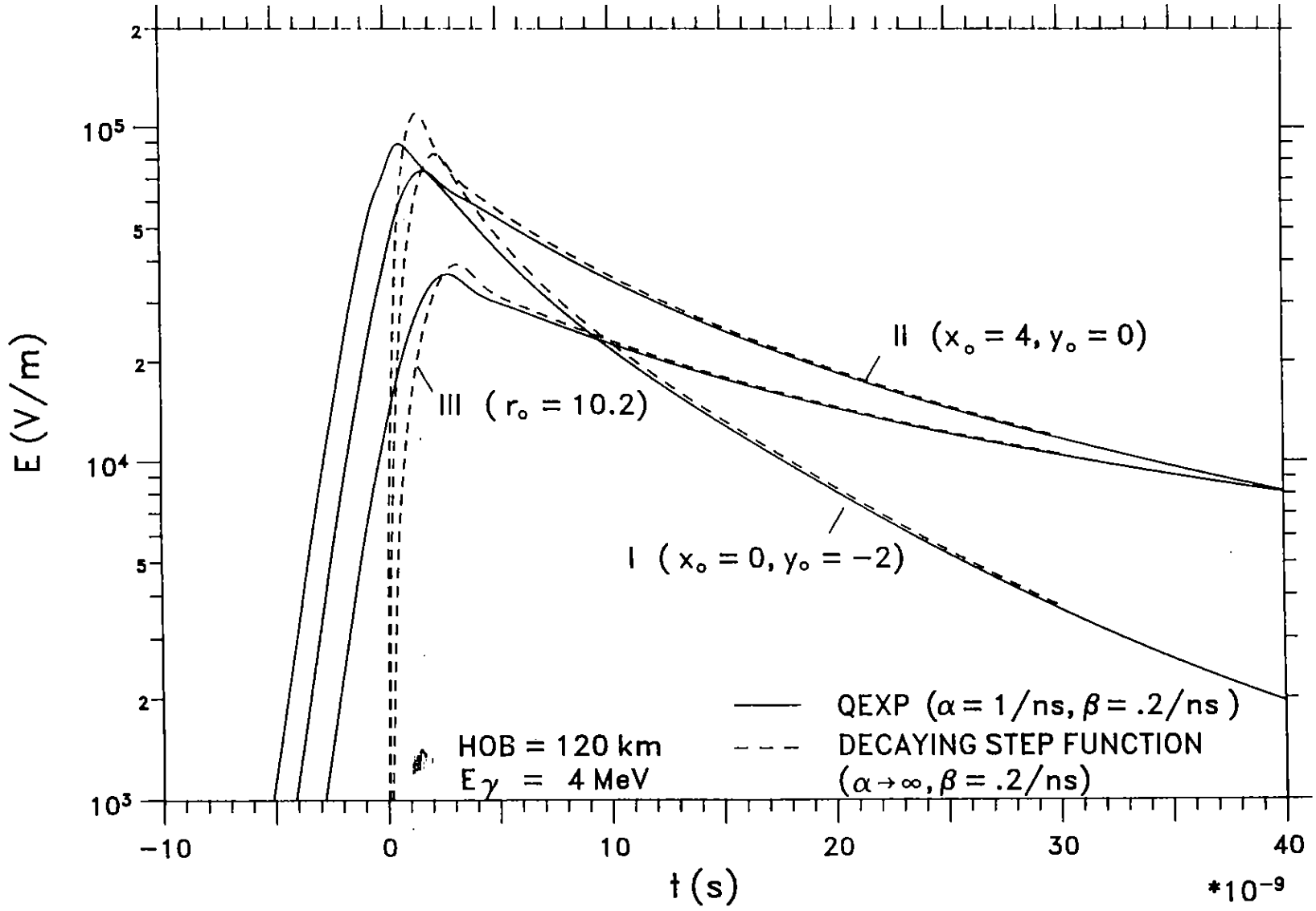

Fig. 24	Total electric fields at 3 different observer locations: (I) maximum peak field, (II) max energy density of .11 J/m^2, (III) explosion horizon (in units of HOB)